»Development of a high-resolution spectrograph and observations of CH^+ absorption lines in the interstellar medium«

von
Ingo Steiner
aus
Hadamar

Bochum 2008

Dissertation zur Erlangung des Grades
»Doktor der Naturwissenschaften«
der Fakultät für Physik und Astronomie
der Ruhr-Universität Bochum

1. Gutachter: Prof. R. Chini
2. Gutachter: Prof. A. Quirrenbach
Datum der Disputation: 27.01.2009

Abstract

This thesis consists of two parts. The technical chapters document the development of the high-resolution spectrograph BESO for the Hexapod-Telescope at the Cerro Armazones Observatory, Chile. The observational chapter researches specific properties of the interstellar medium.

Starting from the requirements for a new spectrograph, the design of FEROS, a very successful instrument at the European Southern Observatory (ESO), is discussed. The required modifications to adapt the design of FEROS to the installations at the Cerro Armazones Observatory are presented. In regard to ongoing technological development updates are discussed to make use of technology developed since the design of FEROS.
The manufactured components and the complete system were tested to ensure that all components function as specified and that the defined performance of BESO is achieved. A first on-sky observation has been accomplished that demonstrates that BESO is ready for scientific observations at the Hexapod-Telescope.

Absorption lines of CH^+ are used to measure the carbon isotope ratio in the interstellar medium of our Galaxy. To study the environment in which CH^+ is formed, high-resolution spectra have been obtained with FEROS at the 2.2 m telescope of ESO and Max-Planck Gesellschaft. A substantial new dataset of CH and CH^+ absorption lines is presented. The sample is coherently processed and compared to other published samples.
On the basis of this dataset several hypothesis are tested to conclude on the environment in which CH^+ is formed. Two subsamples are presented: one with short lines of sight to local stars, and a second subsample with lines of sight within the galactic disc. In our Galaxy more CH^+ is produced along lines of sight towards the spiral arms, where the diffuse photon field is more intense, than along lines of sight in between spiral arms.
The conclusion of the analysis is that CH^+ formation is powered by the diffuse interstellar radiation field. Other hypothetical energy sources for CH^+ production - like turbulence or magneto-hydrodynamic processes - play a minor role.
This result confirms that CH^+ can be used as a tool to measure the carbon isotope ratio in the interstellar medium. The absorption lines of CH^+ allow a reliable measurement of the ^{12}C to ^{13}C ratio. It is shown that these measurements are influenced only up to a few percent by chemical fractionation effects.

Contents

Chapter 1

Introduction

Spectroscopy has a long tradition in Astrophysics. The first spectroscope has been developed by Fraunhofer in 1814 and led to the discovery of absorption features in solar light. 1858 Bunsen and Kirchoff developed the spectral analysis of chemical elements.

Unlike an image where photons of different wavelengths are integrated at every position in the image, spectroscopy records photons separated by wavelength. While the spectrum of a source reveals more information about the physical parameters and processes of the target than an image, imaging resolves the shape and structure of a source at high spatial resolution. The wavelength band used for imaging can be selected using filters. Compared to the resolution of a spectrograph the spectral range transmitted by a narrow band filter is wide and at the edges the transmission function of an optical filter are not steep.

Multi-band cameras for simultaneous imaging deliver an image in several filters at the exactly same time. Today, the most advanced system images in seven bands simultaneously (Greiner et al., 2008). This spectral resolution is coarse - but the spatial and time resolution is very high. This is useful for faint, rapidly changing transients like gamma ray bursts or supernovae.

For technical reasons high spectral resolution generally limits the spatial resolution. A low resolution spectrograph can be combined with an integral field unit to deliver spectra for several hundred positions in a field at the same time. Medium resolution spectrographs can be connected to the focal plane of the telescope with glass fibers recording spectra for up to a few hundred sources simultaneously.

Most low and medium resolution spectrographs record the linear spectrum on a CCD detector. A high number of spectral resolution elements requires re-formatting, so that the spectrum can still fit the detector. A simple way is to split the spectral range in several parts, e.g. a red and a blue half, and to use a seperate detector for each part. To avoid different characteristics of the detectors, the spectral format can be mapped to a two-dimensional plane if high data integrity is required. This is done in an Echelle setup. In such high-resolution systems it is generally not possible to record more than a few spectra at the same time. Ultra-high spectral resolution can only be achieved by limiting the spectral range or by scanning through frequencies.

1.1 Cerro Armazones Observatory, Chile

Cerro Armazones is a 3064 m high mountain located 35 km off the Pacific Coast in the Atacama Desert, 110 km south of Antofagasta in Northern Chile. The observatory has been established by Universidad Católica del Norte that operates a 41 cm and a 84 cm telescope at the site. Ruhr-Universität Bochum has installed the 1.5 m Hexapod-Telescope and the robotic VYSOS 16 (41 cm) and VYSOS 6 (15 cm) telescopes at a peak next to Cerro Armazones.

The VYSOS telescopes are designed to image large parts of the sky every night in order to search for variable objects. The luminosities of stars in the target fields can be measured in several filters. They are stored in a database so that light-curves can be extracted for the "Variable Young Stellar Object Survey" (VYSOS).

To study the physical processes causing variability in the objects discovered with the VYSOS system, a high-resolution spectrograph is required. It is operated as the primary science instrument at the 1.5 m Hexapod-Telescope. The spectral data will lead to a deeper understanding of the processes and mechanisms that drive variability in different categories of stellar objects and active galactic nuclei.

The observatory of Ruhr-Universität Bochum, Germany and Universidad Católica del Norte, Chile at Cerro Armazones is ideally suited to carry out long-term research projects that cannot be performed at public observatories.

The technical work on the high resolution spectrograph for the Hexapod-Telescope supports this ambitious long-term strategy.

	Mirror size	Operation	Designation
VYSOS 6	15 cm	robotic	Optical imaging to cover the complete Milky Way every night
VYSOS16	41 cm	robotic	Optical imaging of selected fields on southern hemisphere
IRIS	80 cm	robotic	Infrared imaging of sources down to 15 mag
HPT	1.5 m	manual	High-resolution spectroscopy down to 16 mag

Table 1.1: Telescopes installed and projected by Ruhr-Universität Bochum at the Cerro Armazones Observatory.

Figure 1.1: Installations of Ruhr-Universität Bochum in the Atacama Desert seen from the peak of Cerro Armazones (3064 m).

1.2 Spectroscopy of the interstellar medium

The discovery of cold diffuse matter in the space between the stars is attributed to Johannes Hartmann in 1904. Spectroscopy of Delta Orionis showed a weak but very narrow Calcium line, that did not shift with the orbital motion of the binary star. It could therefore not originate from the stellar photosphere.

High-resolution spectroscopy of absorption features along lines of sight towards a distant background stars is still the common way to gather information on the properties of the interstellar medium.

The interstellar medium consists of 99% gas and about 1% dust. Electromagnetic radiation forms a diffuse radiation field in the interstellar medium. The interstellar medium is turbulent and interacts in various ways with the stars. Young stars are formed in dense molecular clouds, while stellar winds and shock waves from supernovae transport matter from the stars into the interstellar medium.

One approach to learn about these processes is to study the carbon isotope ratio in different regions of the interstellar medium. Early generations of stars produce only ^{12}C in their fusion process, while later generations also produce ^{13}C.

The most reliable measurements of the carbon isotope ratio use absorption lines of the CH^+ ion that is formed in the interstellar medium. It is assumed that the ratio of $^{12}CH^+$ to $^{13}CH^+$ is equal to the ratio of ^{12}C to ^{13}C. The environment where the CH formation reaction takes place is not completely understood so far and could influence the result of the measurement by chemical fractionation that shifts the $^{12}CH^+$ to $^{13}CH^+$ ratio from the carbon isotope ratio.

The second part of this thesis uses high resolution spectroscopy to further research the environment where the CH^+ molecule is formed to verify the basic assumptions on which the measurement of the carbon isotope ratio is based.

1.3 Objective

In this thesis the development of the high-resolution spectrograph BESO for the Cerro Armazones Observatory is described from the design phase of customized components up to tests of the complete system.
The quality of the components and the assembled instrument is demonstrated. The scientific operability is proved by a first on-sky observation with the spectrograph at the Hexapod-Telescope.

Using high-resolution spectroscopic data, the environment where the formation process of CH^+ molecules takes place in the interstellar medium is investigated. Studies of CH^+ absorption lines are an important tool to measure the carbon isotope ratio in the interstellar medium. These measurements rely on the assumption that chemical fractionation does not significantly change the local isotope ratio from the general value.
This analysis verifies that assumption on a reliable observational dataset and clarifies the basis of the carbon isotope ration measurement on CH^+ absorption lines.

Chapter 2

BESO design

The astronomical institute of Ruhr-Universität Bochum decided to install a high-resolution spectrograph at the Hexapod-Telescope. Located at Cerro Armazones in Northern Chile the instrument is intended for continuous observations of processes in variable stars and galaxies. A versatile instrument combining high spectral resolution, wide spectral range and high photon efficiency is required to provide a useful infrastructure for observing campaigns with various scientific goals.

The instrument is called »BESO«, an acronym for »Bochum Echelle Spectroscopic Observer«. In the following section, the requirements for such an instrument are analyzed. It is suggested to follow the design of the existing spectrograph FEROS, the »Fiber-fed Extended Range Optical Spectrograph« implementing necessary customization and adjustment. FEROS is in operation at the European Southern Observatory (ESO) at La Silla, Chile.

FEROS has been built by Landessternwarte Heidelberg and was installed at the ESO 1.52 m telescope in 1998. It has been moved to the 2.2 m telescope of ESO and Max-Planck Gesellschaft in 2002 and is in continuous science operation. The Landessternwarte has decided to collaborate with Ruhr-Universität Bochum on BESO to extend their options for spectroscopic observation campaigns.

The 1.5 m Hexapod-Telescope has been developed by Vertex Antennentechnik as a prototype for large telescopes based on a Stewart platform mount. It has been installed at the Cerro Armazones Observatory in 2005 by Ruhr-Universität Bochum.

An outlook on BESO has been published in Steiner et al. (2006). A summary on the engineering-modifications and testing results for BESO has been published in Steiner et al. (2008). The as-built drawings and operation instructions are documented in the BESO manual.

2.1 Requirements for BESO

The key task of BESO is to deliver spectra of high resolution with $\lambda/\Delta\lambda \approx 50.000$ over the complete visible wavelength range. Very low noise and the highest possible photon efficiency are necessary to obtain spectra from faint astronomical sources down to 16 mag with a reliable signal-to-noise ratio of better than 10 in one hour.

Because BESO will be installed at the 1.5 m Hexapod-Telescope on Cerro Armazones, a remote location with relatively little infrastructure, it is necessary that BESO can be operated reliably with long maintenance cycles.

The instrument must be designed with a rigid mechanical structure and supported by a vibration damping system to account for vibration from the surrounding building as well as for the frequent earthquakes in the region. The instrument must be shielded from dust and contained in a thermally stabilized room to ensure long-term stability of the instrument performance.

The thermal stabilization requires that BESO is operated without manual interaction by the observer. All settings and commands are entered into the instrument workstation computer that is connected to the instrument hardware. A closed cycle cooling system for the detector is needed to avoid daily refills of liquid nitrogen. Spare parts and all necessary tools must be stored at the observatory to avoid preventable downtime.

The unique design of the Hexapod-Telescope must be taken into account for all components of the instrument interacting with the telescope. The Stewart platform mount of the Hexapod-Telescope limits the space available at the instrument platform of the telescope where the interface flange to the instrument is located. A rigid and light-weight design of all components at the telescope is necessary. It is required that the instrument interface can be removed from the telescope flange within a reasonably short time to allow observations with other, future instruments at the Hexapod-Telescope.

The project to build this high resolution spectrograph has been funded by Alfried Krupp von Bohlen und Halbach foundation with a grant of 600,000 EUR. This gives the upper limit for the total project cost. The goal was to have the new instrument available for scientific observations within three years.

An example for a very successful, efficient high-resolution spectrograph is FEROS that is operated at the 2.2 m telescope at La Silla by the European Southern Observatory. FEROS follows an Echelle design with a prism for cross-dispersion. This principle has been used in several instruments and is regarded as the best approach to combine high-resolution, wide spectral range and high photon efficiency. Because Echelle spectrographs are usually too large and too heavy to be mounted directly at the telescope, they are bench-mounted and connected to the telescope with glass fibers.

2.2 Analysis of FEROS design

FEROS was designed to deliver high resolution spectra with $\lambda/\Delta\lambda = 48.000$, a complete spectral coverage from 370 nm to 860 nm and high photon efficiency of 20%.

FEROS has a high reputation in the scientific community based on its long-term stability. This is achieved through a rigid mechanical design without moving parts inside the instrument, except for one temperature drift compensator. Moreover, the instrument is placed in a thermally stabilized room that is kept at constant temperature. The optical system is set up on a bench equipped with a vibration damping system.

Microlenses are used to couple the light into two glass fibers at the focal place of the telescope. One fiber picks up the light from the science object. The other fiber is used to record the sky background spectrum.

Inside the instrument, the ends of the fibers are imaged onto an image slicer that splits the round image into two halves. The sliced beam has half the height in the direction of dispersion of the grating and twice the width. This way the spectral resolution of the instrument is doubled and all photons from the astronomical source are used. The sliced fiber image is projected on an Echelle grating with 79 lines/mm at 63° angle in Littrow-mode that serves as main dispersing element. The beam is then transferred to a prism for cross-dispersion perpendicular to the direction of dispersion of the grating. The result is a two dimensional echellogram of 39 diffraction orders that is imaged on the CCD detector (Fig. 2.1).

The data reduction software extracts and straightens the curved Echelle orders using flat-field data. Further the software accounts for the order-overlap and outputs two one-dimensional spectra. They are calibrated using wavelength-reference data.

One full range spectrum from 370 to 860 nm is recorded for the sky fiber and one for the object fiber. The sky spectrum can be subtracted from the object spectrum numerically to retrieve the true spectrum of the source.

The requirements for BESO do not interfere with the basic instrument design of FEROS. However, the interface of the fiber-fed spectrograph to the telescope needs to be re-designed because of different mechanical and optical properties of the Hexapod-Telescope. The entrance aperture of BESO can be adapted to the typical seeing conditions at the observatory to increase the signal from an astronomical point source against the background light from the sky (Sec. 2.3).

The space available for the calibration-unit at the instrument platform of the Hexapod-Telescope is limited. The design of the calibration unit for BESO that carries lamps for flat-fielding and wavelength-calibration takes these mechanical constraints into account (Sec. 2.4).

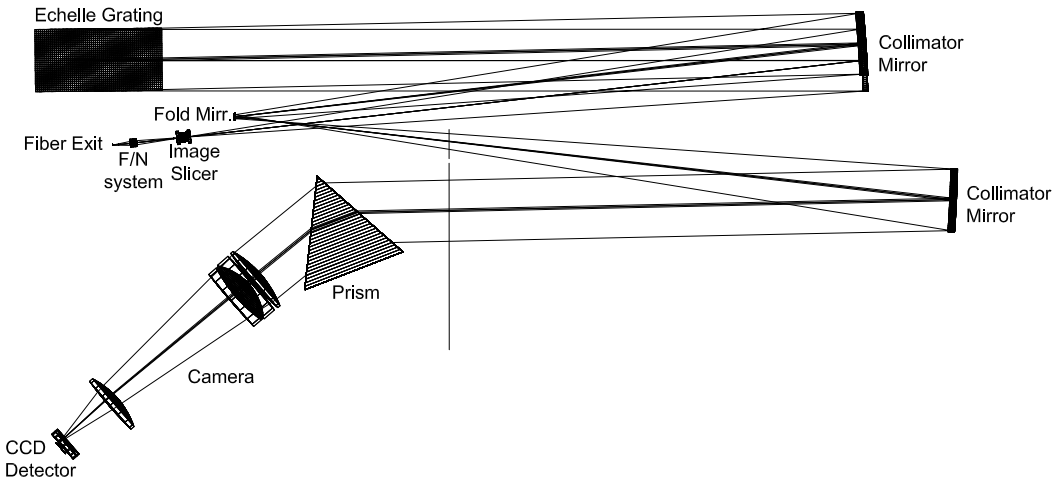

Figure 2.1: Optical layout of FEROS. The light from the fiber exit is sliced and transferred to the dispersion grating. The reflected beam is transferred to the cross-dispersion prism and imaged onto the CCD detector. The dimensions of the optical bench required for this setup are 2.5 x 1.5 m.

A new imaging system is required to avoid liquid nitrogen cooling with daily maintenance. Instead a closed cycle system is used (Sec. 2.5).

An instrument workstation with all software necessary to control the instrument, conduct observations and reduce the data has been included (Sec. 2.6).

All drawings and the complete documentation of FEROS could be obtained from the European Southern Observatory and Landessternwarte Heidelberg. The mechanical design of the instrument needed to be reviewed to ensure completeness and consistency of all drawings. This work was done by Wenli Xu.

The optical design has been re-computed to account for the manufacturing tolerances of the optical components. These computations were done by Walter Seifert of Landessternwarte Heidelberg. Manufacturing drawings have been edited to as-built state by Ludwig Schäffner of Landessternwarte Heidelberg.

The data reduction pipeline has been adapted from FEROS by Otmar Stahl of Landessternwarte Heidelberg.

FEROS was designed and built with state-of-the-art technology in 1996. Meanwhile technological advances have been achieved, which were taken into account while redesigning components. An outstanding difference can be seen in the transmission curve of the glass fibers where significant absorption features have been removed by introducing a technology to manufacture the fibers in vacuum (Sec. 2.3.1).

2.3 Telescope interface

Two glass fibers guide the light from the telescope focal plane into the spectrograph that is located in a dedicated room at the observatory about 20 m away from the telescope. The transmission function of the glass fiber has an important influence on the recorded spectrum. Every fiber attenuates some wavelengths over others. To achieve a smooth transmission function for the whole instrument, a flat transmission function without special absorption features of the glass fibers is required.

The entrance aperture of the fibers needs adaption to the typical seeing conditions at the observatory to increase the signal-to-noise ratio. The focal length of the telescope in connection with the focal length of the microlens on top of the fiber determines the field on the sky from which light is coupled into the instrument (Sec. 2.3.2). The primary mirror diameter and the image quality of the telescope determine the sensitivity of the spectrograph and the telescope.

The image quality of the spectrograph is independent of the image quality of the telescope. Optical and tracking errors of the telescope manifest in the recorded spectra only as a reduced overall sensitivity.

The fiber head forms the mechanical interface to the telescope and holds the glass fibers in the focal plane of the telescope. It is designed to allow quick coupling to the telescope flange in order to allow the use of other instruments at the instrument platform. The fiber head protects the glass fibers against mechanical damage during telescope operation and when the fibers are uncoupled from the telescope.

2.3.1 Fiber selection

Based on the properties of lately developed glass fiber types, the Polymicro FBP multimode fiber was chosen for BESO. The new type has been manufactured in vacuum and lacks the significant absorption feature around 720 nm that was common to earlier silica fibers (Fig. 2.2). The new fiber also shows slightly better overall transmission.

The fiber used for BESO has 100 μm core diameter and 140 μm diameter including the polyamide cladding. Each fiber is protected against mechanical damage by a PVC jacket. The two fibers used simultaneously are bundled in a flexible metal conduit that extends from the instrument to the telescope focus. The metal conduit protects the fibers from mechanical damage during telescope operation.

The fibers were ordered without connectors, because a free fiber end is required at the instrument side of the fibers. The fiber ends have been hand polished to achieve the best possible transmission. The fibers were polished and prepared for assembly with the fiber head by Gerado Avila in the laboratory of the European Southern Observatory in Garching.

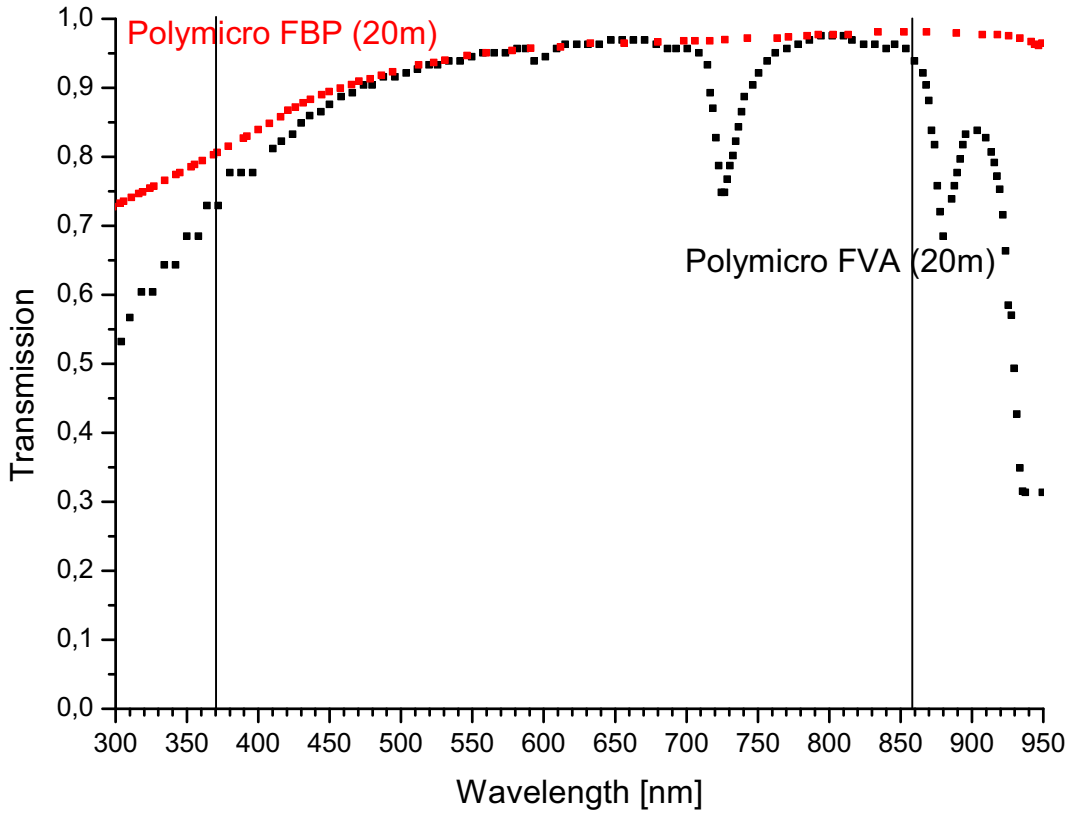

Figure 2.2: Transmission over wavelength for the standard optical fiber (FVA, black) and the new broadband fiber (FBP, red) that has been chosen for BESO. Data from Polymicro Technologies website extrapolated for 20 m fiber length. Vertical lines indicate the spectral range of BESO.

2.3.2 Observational requirements and seeing conditions

The entrance pupil of BESO determines the area on the sky from which light is coupled into the instrument. The entrance aperture of the instrument should have the size of the Airy disc of the source imaged onto the fiber head by the telescope.
If the aperture opening is larger, more background light from the sky is recorded by the object fiber. This light can be subtracted numerically using the spectrum from the sky fiber, but the Poisson-noise of the sky light degrades the signal-to-noise ratio of the science observation. Especially for the observation of faint sources a low background is necessary.
If the aperture opening is too small, light is lost and the overall sensitivity is reduced.
The differential atmospheric dispersion spreads the light from a star into a small angle, forming a vertical spectrum across the entrance pupil. The opening angle of the spectrum depends on the declination. The differential dispersion is 0 for observations in the zenith and increases towards the horizon. When the differential dispersion exceeds the size of the diaphragm the extreme wavelengths (blue and red) cannot be recorded by the instrument (Tab. 2.1).

DEC	350 nm	500 nm	850 nm
90°	0.00	0.00	0.00
72°	0.35	0.00	-0.21
60°	0.62	0.00	-0.37
50°	0.91	0.00	-0.53
40°	1.30	0.00	-0.76
30°	1.90	0.00	-1.12

Table 2.1: Differential atmospheric dispersion in arcsec depending on declination and wavelength. Data computed for ESO's observatory at Paranal. Temp. 11.5°C, air press. 743 mbar, rel. humidity 14.5%. From ESO Astroclimatology website.

Due to the small size of the aperture and the required shape precision, an adjustable iris diaphragm cannot be used. The diaphragm must be aligned with sub-micron precision to the optical axis of the fiber. The absolute position is crucial for the sensitivity of the instrument, so that a movable plate with differently sized holes cannot be used in an instrument aiming at long term stability.
Weather data recorded close to the Cerro Armazones Observatory during 2005 shows a typical seeing below 1 arcsec.
The diffraction limited resolution of the telescope is given by $1.22 \cdot \lambda/D$, with D being the main mirror diameter and λ the observed wavelength. For visual observations with the Hexapod-Telescope the diffraction limited resolution is 0.08 arcsec.
Atmospheric seeing and telescope resolution add up with the differential atmospheric dispersion to the vertical size of the spectrum in the focal plane of the telescope.
Because the flux from the source weakens with higher airmass, science observations are usually not carried out below 40° declination. Therefore the size of the diaphragm was chosen to be 3.4 arcsec projected on the sky or 206 μm in mechanical size.

2.3.3 Fiber head design

Sky and object fiber are held in the focal plane of the telescope by the fiber head. It is mounted at the instrument flange of the telescope. Microlenses are used on top of the fiber ends to couple the light efficiently into the glass fiber. Fibers and microlenses are aligned and glued in the rigid fiber head that allows quick mounting and dismounting when the telescope shall be equipped with another instrument.
Sky and object fibers are separated by 8 mm. This distance corresponds to 2.2 arcmin on the sky. The surface of the fiber head is tilted by 17°. A reflective plate on top of the fiber head serves as diaphragm in front of the microlens and as mirror to control the position of the star on the diaphragm.
All light that does not enter the fiber is mirrored to the fiber viewer camera by the inclined reflective diaphragm. This fast camera monitors the fiber head at about 1 frame/sec and allows to position a star. The star can only be seen until it is positioned exactly on the fiber and all light is guided to the spectrograph. The fiber viewer can be used to track the star and to re-position the telescope when light appears at the inner rim of the diaphragm.

The fiber viewer camera is located outside the telescope beam on top of the instrument platform (Fig. 2.3). It does not disturb other instruments at the telescope flange. Therefore it can remain at the telescope even when other instruments are used.

For BESO's fiber head an "alignment by design" approach was chosen. This means that the mechanical design and the accuracy of the manufactured parts guarantee the alignment of fiber with 100 μm diameter with respect to the microlens with 0.8 mm diameter. The traditional approach is to provide a six degrees of freedom mechanism and to align the microlens with respect to the fiber manually at the cost of a high number of small, moving parts.

The advantage of this approach is that the assembly procedure of the fiber head is very simple and easy, once the parts are manufactured accordingly. The manufacturing process itself is faster, because less and simpler parts are required. Though, the required precision of the parts is higher. All parts in the fiber head are fully locked and cannot move over time. This increases the durability and long-term stability of the fiber head.

A disadvantage of this technique is that the result of manufacturing and assembly are visible only after the complete assembly of the fiber head - which is irreversible as all parts are irreversibly locked in the assembled fiber head.

Because the quality of the alignment essentially depends on the accuracy of the workshop a series of parts has to be manufactured and several fiber heads need to be assembled from the most precise parts.

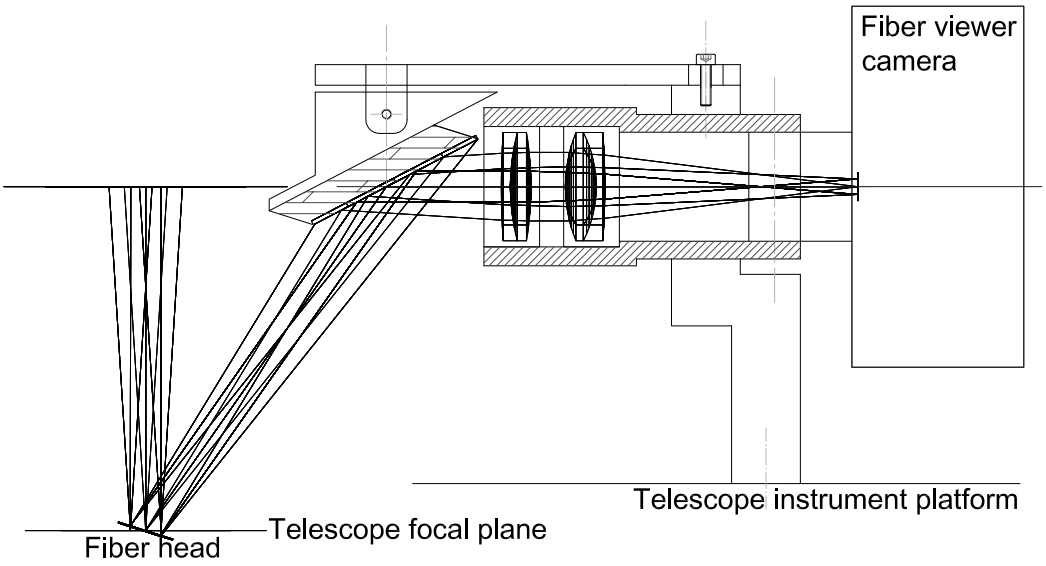

Figure 2.3: Optical and mechanical design of the fiber viewer. The telescope focus and the fiber head are on the bottom left. The camera (right side) images the light reflected from the diaphragm via a simple relay optics.

For efficient transmission of light from the telescope into the fiber, all elements need to be centered on a common axis parallel to the optical axis of the telescope. An offset microlens with respect to the fiber would cause a tilted beam. Fiber, microlens and diaphragm must be in correct distance. An offset of the diaphragm would result in shadowing. All these misalignments would reduce the sensitivity of the instrument.

The tolerances for the alignment of the optical components, that are to be expected from the mechanical accuracy that the workshop can provide, are shown in tab. 2.2. The critical source of error is lens centering, as a de-centering of 10 μm leads to a beam angle of 2° from the optical axis. It is to be expected that the manufacturing tolerances spread following a Gaussian with $\sigma = 10\mu$m. So we can expect 66% of the parts to have less deviation from the required size.

The component qualification (Sec. 3.1) verifies that the necessary accuracy has been achieved. The best performing fiber in a head will be used as object fiber, the other can serve well as background fiber. The relative sensitivities of the two fibers can be measured using the flat-field lamp in the calibration unit.

The assembly of the microlens and the fiber is failsafe and easy. To center the microlens on the glass fiber the fiber end has been glued in a standard FC-connector with ceramic tip and $\pm 1\,\mu m$ radial tolerance (Fig. 2.4, black part). The fiber end has been polished in the connector tip to achieve a flat surface. The outer connector ring has been removed from the connector, so that the centering part (Fig. 2.4, red part) can be put over the tip. The centering part has been machined precisely out of stress relieved aluminum. This part is designed to center the microlens with respect to the FC-connector tip. A small drop of glue and the microlens are inserted into the center hole of the part. The microlens can be pushed down gently until it touches the fiber end. Finally, the optical glue can be hardened by illuminating the fiber with ultraviolet rays.

The assembled fiber end is then inserted into the fiber head (Fig. 2.5). The FC-connectors are pushed upwards and locked by an aluminum plate. The outer fiber jacket is clamped in the fiber head (Fig. 2.6). The fibers including their jackets are protected from mechanical stress by a flexible steel conduit that extends 20 m from the fiber head to the spectrograph room.

	Centering		Focus	
Fiber end	$\pm 1\,\mu$m	Connector ceramics	$< 1\,\mu$m	Polishing under microscope
Lens	$< 10\,\mu$m	Precision drill	$\pm 1\,\mu$m	Surface-to-surface contact
Diaphragm	$< 1\,\mu$m	Manual adjustment	$\pm 10\,\mu$m	Accuracy of CNC-machining

Table 2.2: Alignment errors to be expected from the mechanical accuracy of the machined parts for the optical components in the fiber head.

The movable diaphragm is mounted above the fiber end (Fig. 2.7). The diaphragm for each fiber can be moved separately. The diaphragm consists of a electroformed 20 μm thick plate with a elliptical hole of 215 μm to 206 μm, mounted at 17° angle. The diaphragm is a circle in projection by the telescope beam. Each diaphragm is kept in place by two centering bolts on the outer frame. The outer frame can be moved precisely by two eccentric bolts and locked by two screws.
The adapter ring from the fiber head to the central flange of the Hexapod-Telescope is shown in fig. 2.8. Adjustment rings have been included that can be placed between the fiber head and the adapter to bring the fiber head to the telescope focus within the required tolerance of ± 0.5 mm.

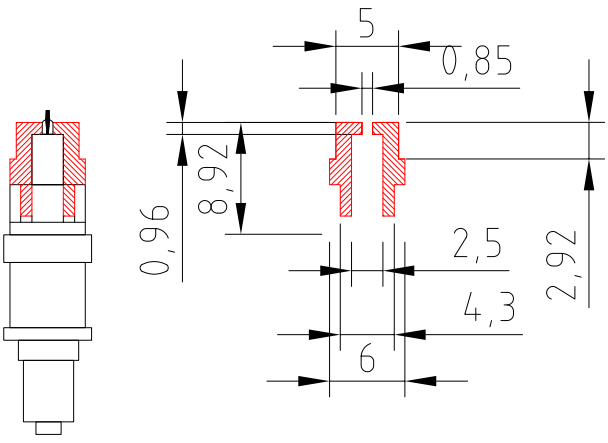

Figure 2.4: Left: FC-Connector (black) assembled with centering part (red) and microlens. Right: Dimensions of the centering part in millimeters.

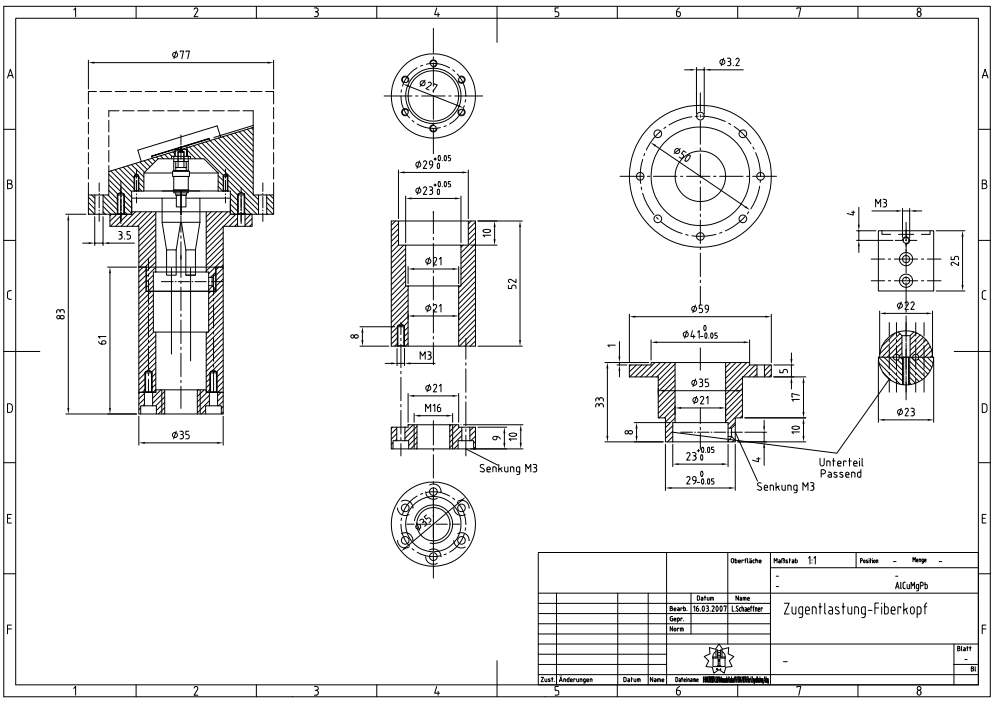

Figure 2.5: Construction drawing of the fiber head (side view).

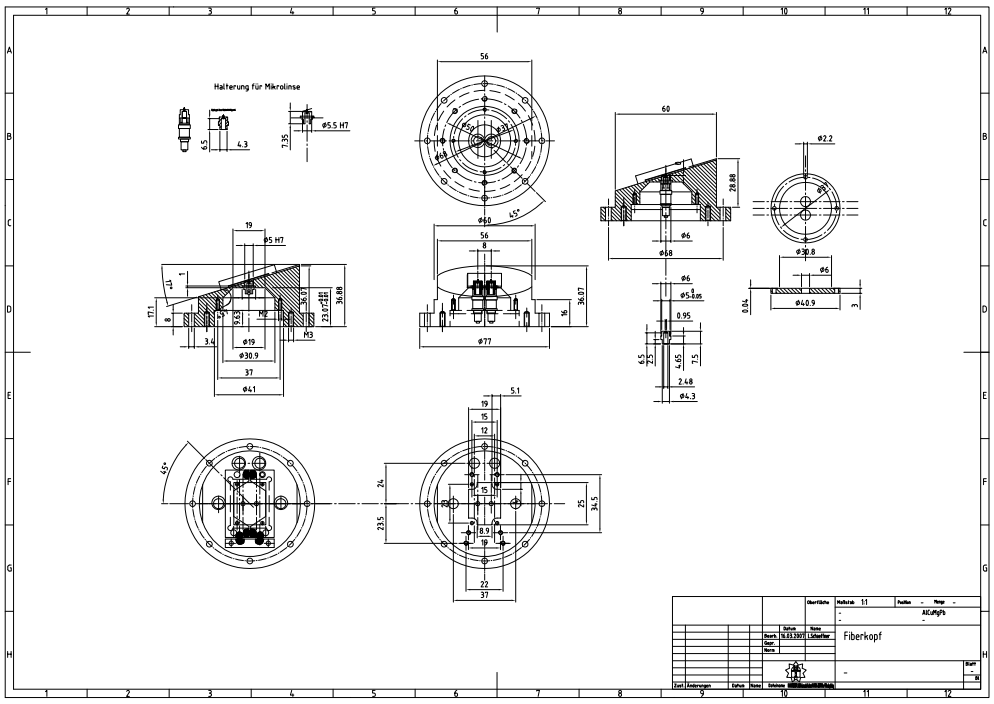

Figure 2.6: Construction drawing of the top cap of the fiber head that hold the fiber ends.

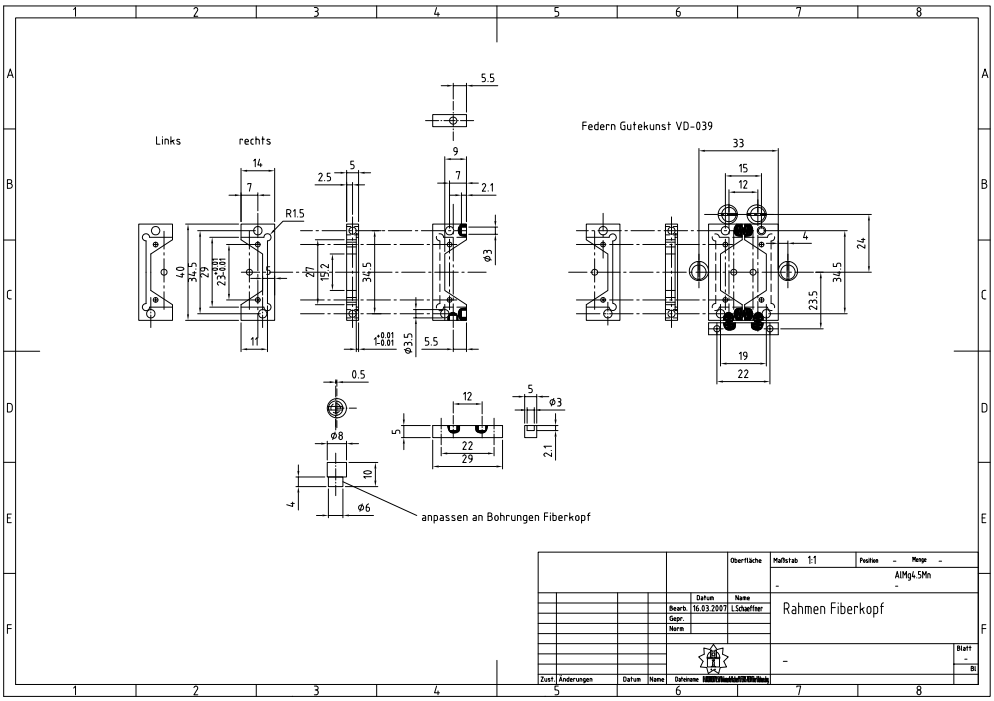

Figure 2.7: Construction drawing of the diaphragm mechanics on top of the fiber head (top view).

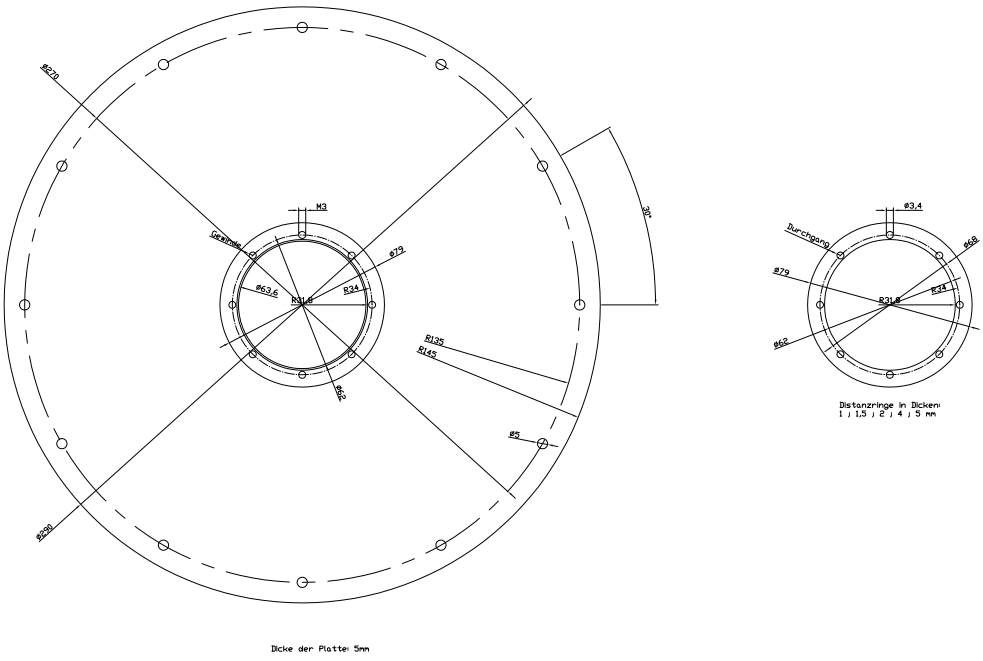

Figure 2.8: Left: Adapter ring to mount the fiber head to the central flange of the Hexapod-Telescope. Right: Adjustment rings.

2.4 Calibration unit

BESO is calibrated using two light sources mounted in one calibration unit. A flat-field source provides white light that enables the data-reduction software to determine the position of the 39 Echelle orders on the detector and allows measuring the relative transmission of the sky fiber compared to the object fiber.

Wavelength calibration is done with an arc lamp that provides a well known line spectrum with usable intensities across the entire wavelength range.

The calibration unit is mounted permanently at the telescope. A retractable arm relays the beam from the calibration lamps into the telescope focus while taking calibration data. The beam from the calibration unit has the same aperture ratio as the telescope and illuminates both fibers homogenously.

A series of calibration frames should be taken at the beginning and at the end of every night.

2.4.1 Flat-field source

The ideal flat-field source would emit light with constant flux across all wavelengths. A flat spectrum is necessary to illuminate all detector pixels along the spectrum homogeneously. A high brightness is desired to get a good signal-to-noise ratio in a short exposure time and to reduce the overhead time for flat-fielding. The task is to filter light from a commercial light source, so that enough flux is emitted at every wavelength covered by the instrument.

Two halogen bulbs with tungsten filaments shall be combined, each emitting a thermal spectrum of 3200 K. By using filters the dominant red part of the spectrum can be suppressed for one lamp resulting in a much more homogeneous combined spectrum (Fig. 2.9).

Most of the light emitted by the lamp will be blocked by the filters. But efficiency is not important at this point, because bright lamps can be used in the permanently mounted calibration source. The calibration lamps are used only for a few minutes at a time, so that their heat does not cause additional turbulence at the telescope.

To find the optimal filter configuration and intensity ratio of the two lamps, a software has been developed to simulate different configurations and to choose the optimal setting.

The optimal filter configuration is determined based on the flatness of the resulting spectrum (minimum to maximum intensity ratio) and overall brightness (integral of intensity over wavelength).

Given 3806 possible filter combinations from the Schott filter catalogue, the following setting has been automatically chosen, taking into account the CCD response function: 20 % intensity with KG3 infrared blocking filter combined with 80 % intensity with KG3 plus BG25 and BG39. The resulting spectrum is displayed in fig. 2.9.

The intensity ratios can be implemented by using 10 and 50 W halogen bulbs with UV-transparent glass.

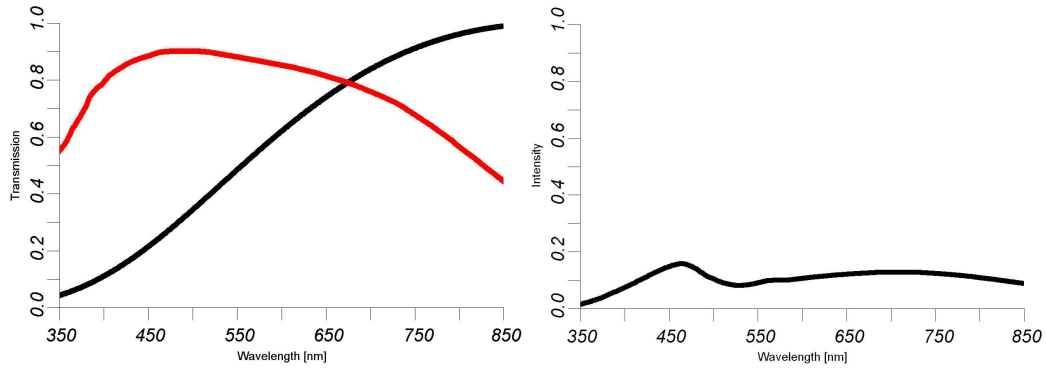

Figure 2.9: Left: CCD sensitivity over wavelength (red) and black body spectrum at 3200 K (black). Right: Computed flat-field spectrum with optimal filter configuration.

2.4.2 Line source

To determine the absolute position of a certain wavelength on the detector, an arc lamp is used that emits a well known line spectrum with bright and narrow emission lines. Neon and argon are used as fill gas with a ratio of 1:10, together with a thorium element. The gas ratio has been chosen to suppress the extremely bright neon lines that quickly saturate the detector before weaker lines are recorded with sufficient signal-to-noise ratio. The thorium element adds lines at the blue end of the spectrum that is not sufficiently covered by neon lines.
Fig. 2.10 shows the spectra of the three elements used in the calibration source. The spectrum is measured with BESO (Sec. 3.2, Fig. 3.2).

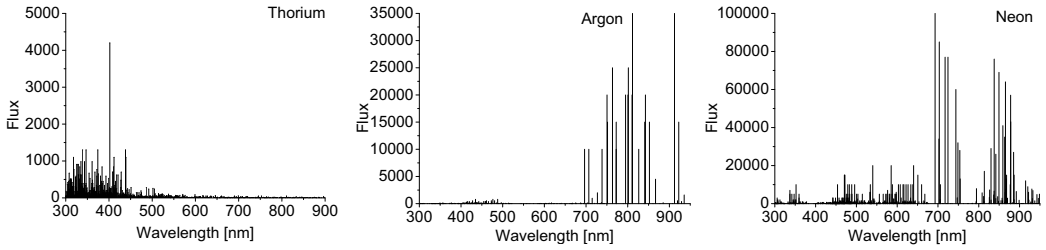

Figure 2.10: The plots show the spectrum as flux over wavelength for thorium (left), argon (center) and neon (right). Data source: National Institute of Standards and Technology website.

2.4.3 Optical design

The optical design of the calibration source has been designed by Walter Seifert. The filtered light from two halogen lamps with 10 and 50 W is combined with a 50:50 beam combiner and imaged by relay optics to the telescope focus. The light from the arc lamp is imaged to the telescope focus in the same way. A movable mirror selects the light from the halogen or the arc lamp. In the telescope focal plane, both fibers are evenly illuminated by a beam that has the telescope aperture ratio. Fig. 2.11 shows the schematic layout with one calibration lamp.

2.4.4 Mechanical design

The mechanical design was limited by the small space available at the instrument platform of the Hexapod-Telescope. All lamps, optics, motors and electronics are stacked in a small box of 405 x 215 x 160 mm. A movable mirror reflects the light from either the arc or the halogen lamps into the relay optics (Fig. 2.11).

The mirror is operated by an electric motor. A second motor moves the relay optics in and out of the telescope beam. The positions are determined by limit switches. A relay board inside the calibration unit switches the low voltage halogen lamps and the motors.

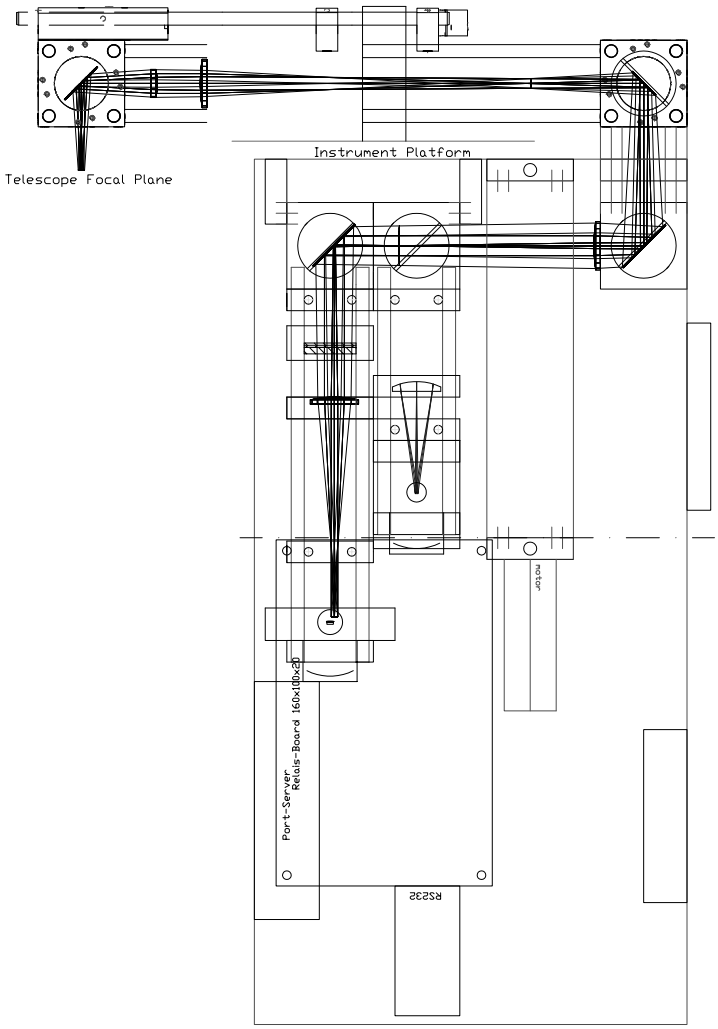

Figure 2.11: Optical and mechanical design of the calibration unit with relay mechanics to the telescope focus.

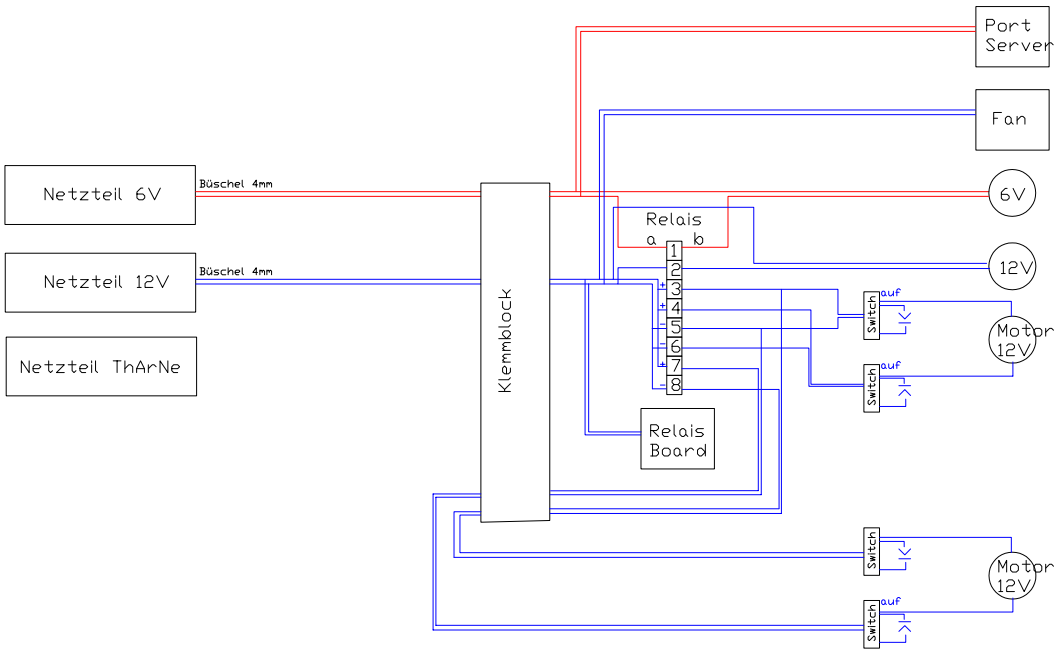

Figure 2.12: Electrical design of the calibration unit.

2.4.5 Electrical design

All low-voltage motors and lamps are switched by an 8-channel relay board. The relay board receives commands via RS-232 serial link through a port server that communicates with the instrument workstation computer via Ethernet.
All commands are echoed back to the instrument workstation, so that the software can verify that a command has been received, properly executed, and that the calibration unit is in a valid state of operation.
The calibration lamps require 6 V and 12 V for the halogen lamps, and high voltage for the arc lamp. The relay board uses 12 V power, the motors and the port server use 6 V. The transformers are located away from the telescope, so that only an Ethernet cable and three power cables have to be connected to the calibration unit. The commanding software takes care that only valid states are switched. The high voltage for the arc lamp is switched externally. Fig. 2.12 shows the wiring scheme.

2.5 Mechanical interface of the imaging system

The CCD detector recording the spectrum is mounted inside a dewar and cooled with a closed cycle system. The detector is wired to the readout electronics. A short distance between the detector and the electronics reduces pickup of external noise in the system. The electronics is attached to the dewar and is air cooled. To keep the turbulent air outside of the optical path, the whole group is mounted outside the instrument enclosure.

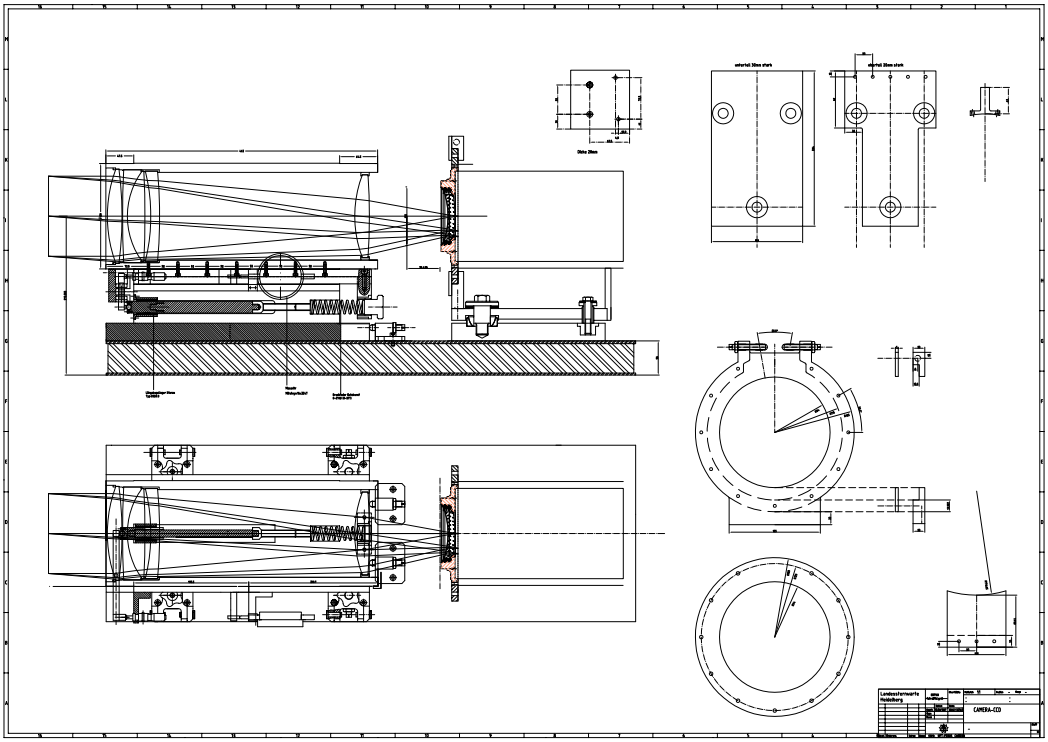

Figure 2.13: Construction drawing of the mechanical interface of the imaging system.

The entrance window of the dewar is the last lens of the camera. Therefore the mount of the dewar must be adjustable to allow precise alignment with the camera. The dewar must allow rotation around the optical axis to align the detector to the curved Echelle orders.
The detector inside the dewar can be aligned independently to the optical surface of the entrance window.
The design of mechanical interface to the dewar is shown in fig. 2.13. The base plate can be positioned freely on the optical bench and adjusted for tip and tilt. The dewar can be rotated $\pm 10^{\circ}$ around the optical axis and clamped with screws. The weight of the coolant lines is held by the right support.
For vibration insulation and thermal decoupling of the shutter coil, the shutter is mounted on the instrument enclosure (not drawn in fig. 2.13). The shutter is connected to the window of the dewar with a light-tight bellow.

2.6 Software

The software for BESO must handle exposure control, CCD readout, and remote control of the calibration source. A data reduction pipeline that converts the data from the CCD detector into spectra is necessary to facilitate the work of the observing astronomer. An exposure time calculator is required to plan observations. It should be accessible on a website.

In order to shorten software development time, it was reasonable, to rely either on purchased software, or on software already developed for FEROS, where available. The software used for the instrument should be documented with its source code, so that future customization of the software is possible.

All software, except the exposure time calculator, is installed on the instrument workstation computer. Its operating system is Windows XP, hosting a Cygwin Linux subsystem. The instrument workstation is located in the control room of the observatory next to the control computers of the telescope. This allows the observing astronomer to operate the telescope and the instrument at the same time.

2.6.1 Exposure control and CCD readout

The manufacturer of the CCD readout electronics delivered their own CCD control software "Voodoo". This software drives the iris shutter for exposure control and the electronics that controls the CCD temperature and the readout process.

Voodoo is written in Java and uses a compiled native package to access the fiber-optic link hardware that connects the instrument workstation to the readout electronics. The fiber optic link galvanically isolates the CCD electronics from the instrument workstation and provides fast data transmission rates.

The instrument specific parameters are loaded from a configuration file. Voodoo's graphical interface can be used straight-forward by the observing astronomer to set the exposure time and trigger the shutter.

The data read from the detector is stored as FITS-file on the hard disk of the instrument workstation. The "Flexible Image Transport System" (FITS) is commonly used to store astronomical data. When a new file is written on the hard disk, a script connects to the telescope control computer to obtain the current coordinates of the telescope. The coordinates are stored together with the instrument parameters of the spectrograph in the header of the data file for future reference.

The files written by Voodoo are processed by the data reduction software to extract a wavelength calibrated spectrum for the user.

2.6.2 Calibration unit control

To remote control the calibration unit, a newly developed software sends commands to the relay board inside the calibration unit at the telescope. The software verifies from the echo of the relay board that the commands have been received. Subsequently the software queries the state of the relay board to verify that the command has been executed and that the calibration unit is in a valid state.

This software has been written in Java to use the same technology that has been used for the CCD readout software in order to facilitate future customizations.

The graphical interface of the software on the instrument workstation enables the astronomer to command the calibration source into one of its three possible states:

1. All off (focus mirror retracted, all lamps off)
2. Flat-field (focus mirror in telescope focus, halogen lamps on, arc lamp off, internal mirror down)
3. Wavelength calibration (focus mirror in telescope focus, halogen lamps off, arc lamp on, internal mirror up)

Beside the three-state user interface, the software also features an engineering mode that allows switching all relays separately.

2.6.3 Exposure calculator

To plan observations, a CGI-script from Landessternwarte Heidelberg was adapted to BESO's instrument properties. This exposure time calculator enables the user to calculate the expected signal-to-noise ratio for a given object brightness and exposure time.
This script is particularly useful to test which exposure time is needed to conduct a certain observation and to estimate the signal-to-noise ratio for a given object at various environmental conditions, like moon phase and atmospheric seeing.
The script is accessible from the website of Ruhr-Universität Bochum. It can be used to plan observation campaigns before arriving at the observatory. Using a web browser, it can also be accessed from the instrument workstation (Fig. 2.14).

2.6.4 Data reduction

To extract spectra from the recorded data, a software pipeline based on MIDAS was chosen, because it is a proven, stable system with ongoing support. MIDAS includes routines to reduce the two-dimensional FEROS echellograms to one-dimensional spectra.
During data reduction MIDAS first evaluates the flat-field to determine the position of the Echelle orders of both fibers on the detector. The corresponding pixels are extracted from the science image, the curvature is straightened, the order-overlap averaged. The orders and the pixels are summed-up over the width of each Echelle order.
The output is a one-dimensional full-range spectrum for each fiber. A correction for the heliocentric motion of the earth can be applied.
Adjustments of the routines to BESO have been done by Otmar Stahl of Landessternwarte Heidelberg. Details of the procedures can be found in Stahl et al. (1999).

BESO Exposure Time Calculator

The calculator computes the S/N per pixel (1 resolution element = 2.2 pixels) for a given exposure time.
Calculations are based on measured performances during the FEROS Commissioning.

Object	**Observing conditions**	**CCD**
Magnitude in V: 12	Moon brightness: grey	readout noise (electrons): 4.2
spectral type: O	seeing (arcsec): 1.5	dark current (electrons/hour/pixel): 88.0
reddening E(B-V): 0.0	airmass: 1.5	full well capacity (electrons): 115000
Exposure	Temperature (centigrade): 15	**Telescope**
Exposure time (sec): 600	atmospheric pressure (hPa): 773	mirror diameter (cm): 150
Number of fibers: 1 2	relative humidity (percent): 25	telescope efficiency: 0.6

Display result | Reset all fields

Expected S/N per pixel in UBVRI					
	U	**B**	**V**	**R**	**I**
Flux from star (electrons/bin)	52	1486	1135	924	480
Flux from sky (electrons/bin)	0	2	2	4	4
Dark current (electrons/bin)	191	191	191	191	191
Readout noise (electrons/bin)	15	15	15	15	15
Expected S/N (per pixel)	1.7	30.8	25.5	22.0	13.2
Additional information					
The slit losses due to the seeing are 2.9 percent.					
0.1 percent of your CCD pixels (1.8 percent of your wavelength bins) are hit by cosmic rays.					
atmospheric refraction: 50.0 arcsec at lambda = 3600 Angstrom, 48.1 arcsec at lambda = 9200 Angstrom length of spectrum = 1.9 arcsec, fiber diameter = 3.4 arcsec					

BESO documentation

Figure 2.14: Screenshot of the exposure time calculator for BESO.

Chapter 3

BESO qualification

After the design phase, the manufactured components have been tested to ensure compliance with the allowed tolerances. The following sections describe the test bed setups and verification procedures.
A test of the complete system has been carried out in the laboratory in Heidelberg to make sure that the instrument delivers the expected performance before it is disassembled and transported to the observatory.

3.1 Telescope interface

To verify the alignment of the optical components in the fiber head, both free fiber ends have been illuminated with a laser. The laser light exiting the fiber head is projected on a screen (Fig. 3.1). Measuring the distance between the projections of the two fibers allows determining the angle between the two beams. Rotating one fiber end in the fiber head allows measuring the angle of the single beam against the optical axis. The method allows an accuracy of $\pm 0.5^\circ$, because the beam exits the microlens with a wide angle.
Two fiber bundles with two fibers each were assembled from selected parts. Two of the four fibers did not show any beam deviation from the optical axis. The two other fibers showed a beam deviation of 2° and 5° from the optical axis.
In the mechanical design (Sec. 2.3.3), the microlens centering on the FC-connector was expected to be the dominant source of alignment error. Two fibers were found to be well aligned with de-centering $\ll 10\,\mu$m and two more with $10\,\mu$m and $26\,\mu$m de-centering.
The deviation between the two beams can be reduced slightly by rotating the FC-connectors in the fiber head. The best aligned fiber in each pair will serve as object fiber. The other as background fiber. The best bundle will be installed at the telescope, the other serves as spare part.
The fiber head has been tested at the telescope using the same method. The fiber head was mounted at the telescope flange. The instrument side of the fiber has been illuminated with a laser. The light exiting both fibers fully illuminated the surface of the secondary mirror of the Hexapod-Telescope.

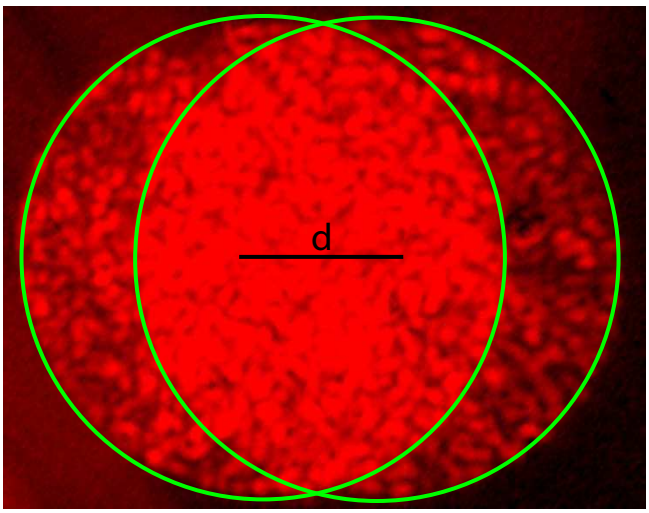

Figure 3.1: Projection of laser light exiting the fiber head on a screen. From the distance d of the center of the two projections the angle between the two beams has been be measured.

This test made sure that a possible tilt of the beam is within acceptable limits and does not affect the sensitivity of the instrument. The test also confirmed the function of the adapter plate that connects the fiber head to the telescope.

3.2 Calibration unit

While testing the instrument in the laboratory and during installation at the observatory the calibration source has been used to align and calibrate the instrument.

In flat field mode, the whole spectral range is illuminated with sufficient signal in the blue end of the spectrum. All 39 Echelle orders can be traced by the automatic reduction procedure. Fine tuning is possible by adjusting the voltage of the power supplies. The source is sufficiently bright to record a flat-field with few seconds exposure time.

The arc lamp provides sufficient lines over the whole spectral range to perform precise absolute calibration of the instrument. The automatic reduction procedure uses 622 emission lines from the thorium-argon-neon spectrum. The spectrum of the arc lamp recorded with BESO is shown in fig. 3.2. The narrow emission lines of the arc lamp are useful to determine the resolution and the focus of the instrument. An exposure time of 60 seconds is required to record a wavelength calibration frame.

The CCD readout takes 40 seconds. A series of flat-field and wavelength calibration files can be recorded in approximately 15 minutes. The calibration data can be taken before and after the observation in the closed dome.

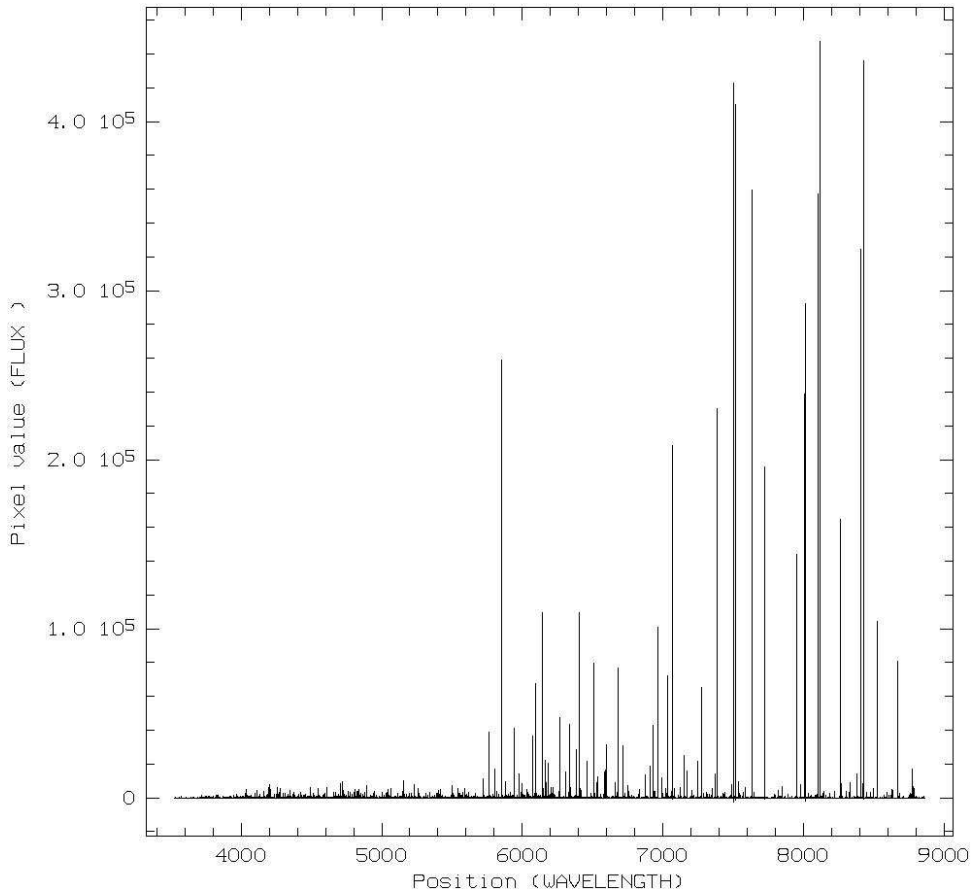

Figure 3.2: Spectrum of the arc lamp used for wavelength calibration (intensity in ADU over wavelength in Ångström). The weak lines at the blue end of the spectrum can be detected by the data reduction software before the stronger lines on the red end saturate the detector.

3.3 Imaging system

The instrument performance for weak sources depends heavily on the quality of the CCD detector and the readout electronics of the imaging system. The readout noise from the detector and the electronics, that is present in every pixel, competes with the flux from an astronomical source that is dispersed over 800,000 pixels.

To determine the limits of the imaging system and their impact on the quality of the science data recorded with BESO, qualification tests have been carried out with the imaging system. Several improvements of the system have been worked out together with the manufacturer of the electronics in order to achieve the best possible data quality.

The components of the imaging system - dewar, cooling unit, electronics and CCD - have been ordered as a bundle from Astronomical Research Cameras Inc. The components have been manufactured by different suppliers.

3.3.1 Image quality

The CCD is a back-side illuminated detector from e2v with 4096 x 2048 pixels of 15 μm each. For the surface an astronomy broadband coating has been used. The detector features simultaneous two-sided readout through two amplifiers. The readout electronics consists of two 16 bit A/D-converters. Both readout channels have been tested. For science observations the detector is read out using only one channel. This avoids problems with slightly different amplifier characteristics and converter offsets. Considering the long exposure times with BESO, typically several minutes, the additional 20 seconds overhead time for using only one readout channel is negligible.
The initial test images taken at the laboratory of the Astronomical Research Cameras showed ghost images (Fig. 3.3) from cross-talk of the two separate read-out amplifiers and a scratch (Fig. 3.4). The cause of the cross-talk was found to be a circuitry error in the readout electronics that could be corrected. The scratched CCD has been replaced by the manufacturer.

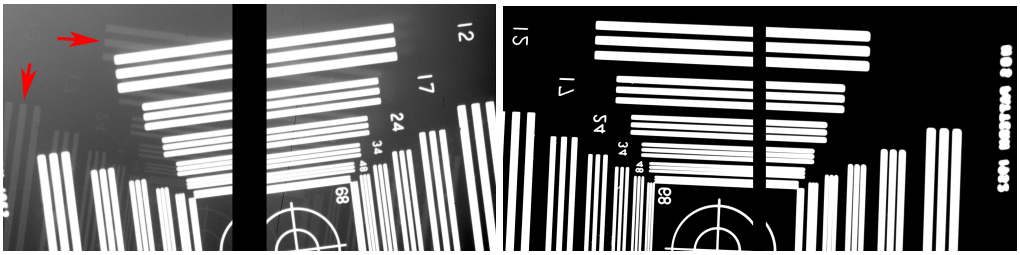

Figure 3.3: Two-sided CCD readout of a test pattern with overscan area in the middle. Left: A mirrored ghost image is visible at approx. 10 % brightness (marked by red arrow). Right: Image taken after fixing a circuitry error in the readout electronics. The ghost image has disappeared.

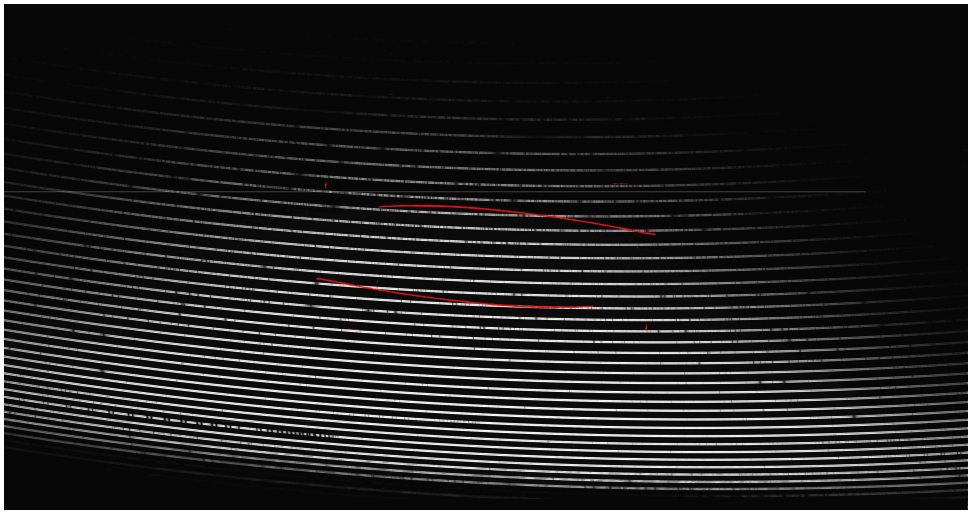

Figure 3.4: The image shows how the scratch (red overlay) on the CCD would have affected the recorded spectrum. The two red curves show the scratch in the two possible ways of mounting the detector.

3.3.2 Gain, linearity and noise

The amplifier gain of the CCD readout electronics is the conversion factor from the arbitrary analog to digital converter units (ADU) to electrons physically moved by light hitting the detector. The knowledge of this conversion factor is important when calculating the physical flux from an astronomical source.

The gain has been measured at an operating temperature of -100 °C by illuminating the detector with a constant light source and taking exposures with various exposure times. Plotting the measured signal against the variance of the signal gives the conversion factor. This is based on the nature of light, that the photon distribution follows Poisson statistics.

The slope of a linear fit (Fig. 3.5) gives the conversion factor in e^-/ADU. The offset of the linear fit gives the readout noise of the electronics.

A third quality measure can be derived from the same plot. Looking at the high signal end of the plot, the signal-to-variance relation is non-linear above a certain number of electrons released in one potential well of the semiconductor material. For scientific observations a non-linearity of up to 1% is acceptable. This limits the usable range of the detector to signals up to approximately 50,000 ADU from the 65,536 ADU (16 bit) available.

Due to manufacturing tolerances both amplifiers in the system show slightly different gains (Tab. 3.1).

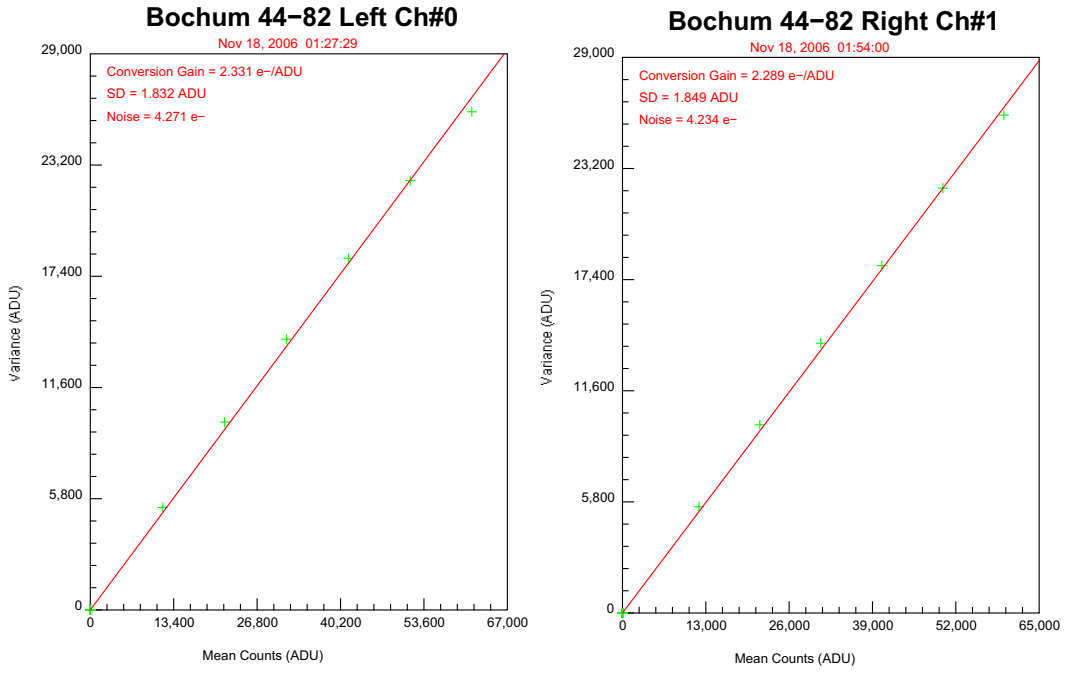

Figure 3.5: Gain measurement for left and right A/D converter. Error bars are smaller than the data point symbol (green) due to the large number of pixels used for this measurement. The red line denotes a linear fit to the data points.

To make sure that the noise of the system is fully random, a Fourier analysis on the dark frames has been run. No pattern has been found in the manufacturers laboratory in San Diego, USA and the laboratory in Heidelberg, Germany. An analysis of dark frames taken at the observatory shows two pickup frequencies close to 30 and 50 Hz slightly above the white noise level (Fig. 3.6). This noise is at a very low level and does not affect the science data significantly.

	Left converter	Right converter
Gain	2.331 e^-/ADU	2.289 e^-/ADU
Noise	4.271 e^-	4.234 e^-

Table 3.1: Gain and readout noise (significant decimals) of right and left amplifier channel.

Temperature	Dark current	Dark current
-100°C	41.4 ADU/h	96.5 e^-/h
-110°C	31.9 ADU/h	74.4 e^-/h
-120°C	7.9 ADU/h	18.4 e^-/h

Table 3.2: Dark current measurement for several operating temperatures of the CCD. The use of 20 frames with $8 \cdot 10^6$ pixels results in an uncertainty of $\pm 0.03\, e^-/h$.

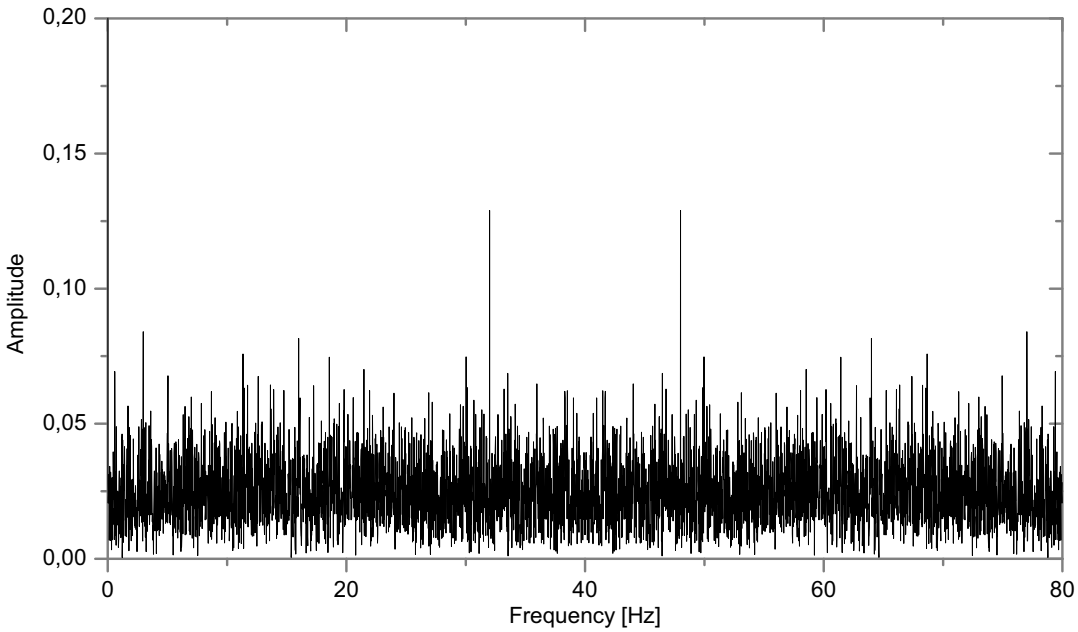

Figure 3.6: A Fourier-Transform of one column of a dark frame recorded at the observatory shows a noise pickup - probably from the power grid. Two frequencies close to 30 and 50 Hz show slightly above the general noise of the system. Noise pickup has not been found during tests at the manufacturers laboratory or at the laboratory in Heidelberg.

Manufacturers test data	99.9996 %
Right amplifier CTE	99.999890 % $\pm 5 \times 10^{-8}$
Left amplifier CTE	99.999891 % $\pm 5 \times 10^{-8}$

Table 3.3: Manufacturers test data (first line) and our CTE measurement (below). After clock pattern improvement, the specification had been reached.

3.3.3 Dark current

The dark current consists of the electrons that are moved into the valence band of the semiconductor material of the detector due to their thermal energy. This current depends heavily on the temperature of the detector and must be subtracted from long-term exposures.

The dark current has been measured by taking 10 dark frames with 600 seconds exposure time and subtracting 10 frames with 0 seconds exposure time to subtract the read-out noise.

The dark current of our CCD for different temperatures is shown in Tab. 3.2. The dark current can be reduced by operating the detector at lower temperatures. But this reduces the quantum efficiency of the detector at the same time. For long observations the dark current, which is very stable over time, can be subtracted numerically from the spectrum.

3.3.4 Charge transfer efficiency

During readout, the electrons moved into the valence band of the detector by the photons are shifted from one pixel to another until they reach the readout electronics connected to the last pixel of the detector. The probability that one charge is transferred from one pixel's potential well to the next is called charge transfer efficiency (CTE). Regarding the size of the detector with 4096 lines, it is obvious that the CTE needs to be very close to one, because otherwise the image quality would be degraded.

The CTE can be measured from the overscan area of an homogenously illuminated image. The overscan pixels are A/D converter samples after the last pixel in a detector row and should only show the noise of the electronics. If the CTE is excellent, the value of the first overscan sample after a bright CCD pixel should be on noise level. Otherwise the sample value will be $(1-\mathrm{CTE}) \cdot n_e$ above noise level, where n_e is the number of electrons in the last pixel. If the CTE is poor, a point source on the CCD shows a trail in the image. From a large number of overscan pixels the CTE can be calculated precisely.

The system showed very poor CTE during acceptance testing. Pixel hit by cosmic particles showed visible trails in readout direction (Fig. 3.7).

As a solution the readout clock-pattern was modified to better suit the CCD. Final inspection of a homogenously illuminated flat field, read out via both readout amplifiers, showed the CTE measurement to be within specifications of the manufacturer (Tab. 3.3).

Left and right amplifier show the same CTE. This is to be expected as only the clocking sequence is altered to change readout direction. The timing values, that affect the charge transfer probability, are the same in both directions.

3.3.5 Residual images

While working with the system, the CCD has repeatedly been exposed to bright light sources beyond saturation. In some systems, residual charges remain in the semi-conductor material and affect the following exposures.

Residual patterns have not been found in images taken after the CCD was cleared. Clearing the CCD is performed automatically by the control software before each exposure. It can also be triggered manually through the graphical user interface of the software.

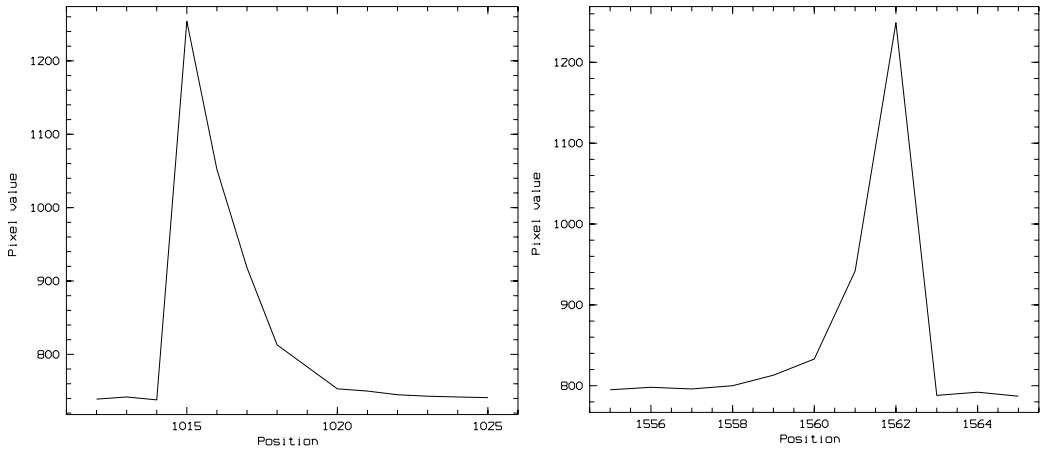

Figure 3.7: Degraded image quality by poor CTE. A point source - in these cases a hit from a high energy particle - leaves a trail. Left: Readout to left converter. Right: Readout to right converter.

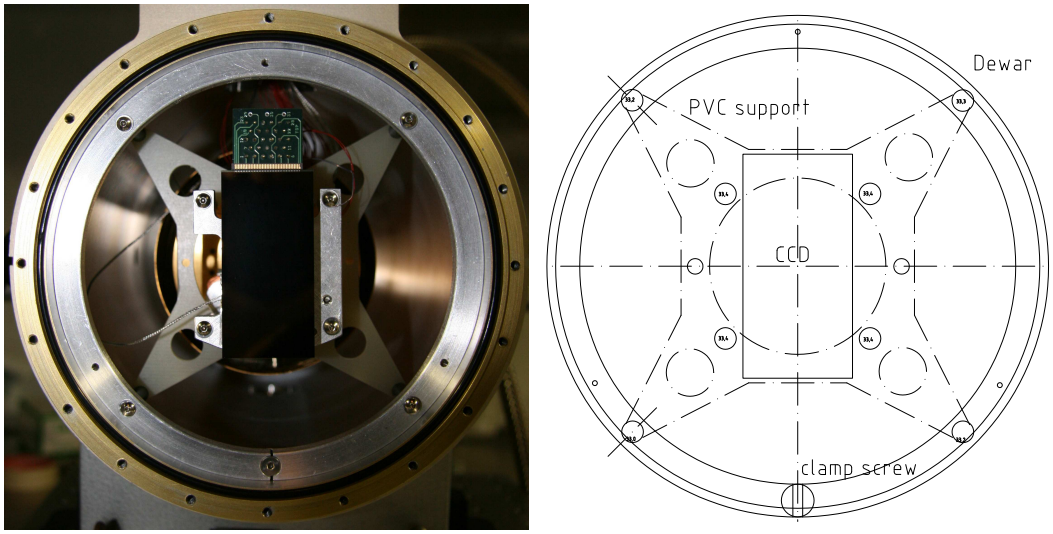

Figure 3.8: CCD mount inside the dewar - as photographic image (left) and drawing (right). A special tool had to be manufactured to reach positioning of the CCD within $\pm 5\mu$m of the focal plane of the instrument.

3.3.6 CCD mount

The mount of the CCD inside the dewar consists of a PVC structure that is screwed to an aluminum ring, which is expanded against the outer wall of the dewar with a screw (Fig. 3.8). This mount allows only coarse adjustment of the CCD position. The alignment precision required for BESO is $\pm 5\,\mu$m in the focal plane of the instrument.
To align the detector, the mount was measured and an adjustment tool was designed that allowed precise movement of the clamped ring, so that an accurate alignment within the tolerances could be achieved. The alignment was verified measuring the distance of the CCD to the inner surface of the entrance window with a microscope.

3.3.7 Cryo system

The operating temperature of the detector can be set through the control software. The temperature reading drifts less than a few tenth of a degree Celsius during operation. The dewar initially showed slight leakage which could be fixed by replacing the seals. An additional cold shield has been added to block thermal emission entering the front window (Fig. 3.9). Once the dewar has been evacuated the system remains stable down to -135°C over several weeks with continuous cooling by the closed cycle cooler.
The dewar initially showed some strange contamination (Fig. 3.10) that condensed on the CCD surface and produced a bluish haze. The source could not be identified clearly. After cleaning the dewar, replacing the cold head of the cryo system, heating and extended pumping the contamination did not reappear.

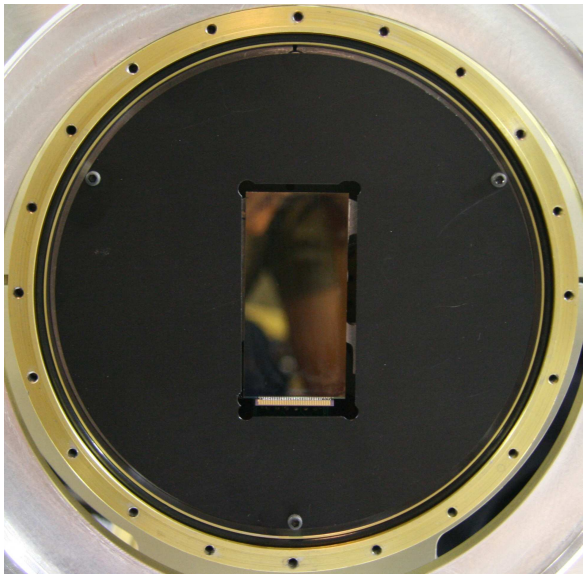

Figure 3.9: Anodized cold shield for the dewar. The additional cold shield improves the thermal stability of the detector inside the dewar.

Figure 3.10: Contamination in the vacuum causing a bluish haze on the cold CCD surface before the cold head has been exchanged.

3.4 Software

The software for BESO has been used extensively during the qualification period. The CCD readout software Voodoo provides the necessary functions. Some minor changes seem desirable to facilitate the work for the observing astronomer. Currently the detector temperature and the direction of readout need to be set manually at every start of the software. The detector temperature reading on the user interface is not updated automatically and the temperature at the time of readout is not properly saved to the header of the data files.
The calibration unit control software conforms to the requirements. The control software for the calibration unit switches the lamps and moves the internal mirrors to switch calibration lamp beams. An extension of the software that automatically finds the network address of the port server in the calibration unit is desirable. Currently this address that rarely changes has to be set manually.
The telescope coordinates are inserted into the FITS-header of the data files by an automatic script. This is helpful when applying the heliocentric velocity correction to the extracted spectra.
The exposure time calculator is working with instrument parameters derived from laboratory data.
The MIDAS data reduction has been run on test spectra. The system reduces spectra automatically. Guess tables that describe the position of the Echelle orders on the detector have been prepared by Otmar Stahl. The software uses these initial values to find the Echelle orders in the image. From this starting point the whole reduction procedure for one exposure takes approximately 40 seconds on the instrument workstation.
This allows the observing astronomer to check the recorded data during the observing run and to adapt the instrument settings, if necessary.

3.5 Optical system

The collimator mirrors and the prism have been delivered with interferograms taken by the manufacturers. The deviations from the ideal shape are within the tolerances allowed by the error budget of the optical design.
Both image slicers (one spare part) have been tested in an optical test bed to verify the correctness of the dimensions of the slicers. Imperfections of the slicer edge (Fig. 3.11) are below critical size.
The camera optics has been inspected at the manufacturer prior to delivery. Several mistakes had occurred in the assembly process, which delayed the delivery by several months. The final test data of the camera are well within specifications.
During the setup of the instrument in the laboratory, the image quality has been checked repeatedly against computed spot diagrams to ensure the quality of the F/N-system and the whole setup.
Following an alignment procedure, the optical elements of the instrument have first been positioned on the optical bench with mechanical precision. A coarse alignment has been performed by placing a laser at the position of the fiber exit unit. The laser beam

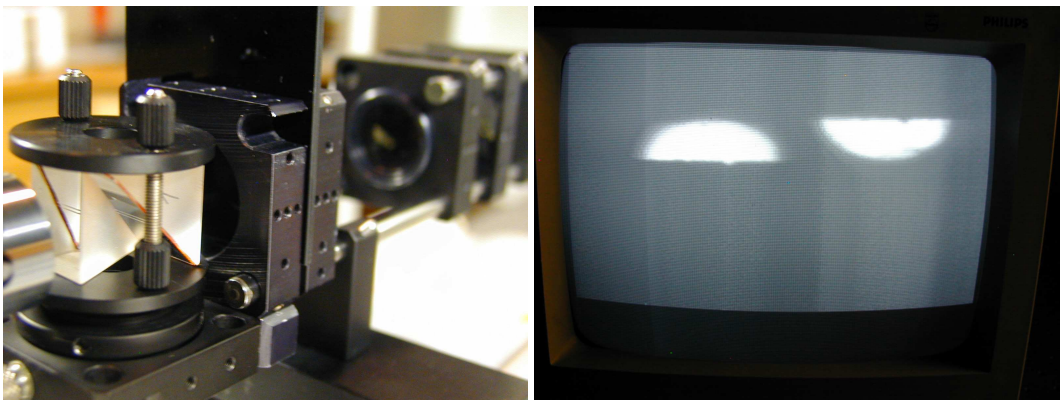

Figure 3.11: Left: Test-bench setup for the verification of the image-slicer. Right: CCD image of one sliced beam. The visible inaccuracies are far below critical size as one slice covers 2.2 x 4.4 pixels on the science detector.

positions have been computed and marked at several points in the system, so that the alignment could be refined successively. Precise optical alignment has been performed using an autocollimator in place of the fiber exit unit. Together with several alignment tools manufactured for the instrument, the autocollimator allowed iterative alignment of all optical components. Final fine-tuning has been performed by measuring the width of narrow spectral lines from the calibration source across the whole CCD detector.
The width of one spectral element in direction of dispersion is 2.2 pixels according to the optical design. The image quality shows a slight gradient over the detector plane. In the laboratory setup the computed image quality has been achieved. In the final setup at the observatory, the image quality in the detector plane slightly exceeds the computed resolution with 1.9 pixels per resolution element at the center of the detector plane.

3.6 End-to-end test

The entire instrument has been assembled and aligned in the laboratory of Landessternwarte Heidelberg. End-to-end tests have been conducted to make sure that all components work well together and that the expected performance can be achieved.
A solar spectrum has been recorded by pointing the fiber head towards the sun on a clear day. Fig. 3.12 shows a small section of this spectrum around the CaII-line. The spectrum has been reduced using MIDAS not taking into account calibration data. This leads to an arbitrary offset on the wavelength and intensity axis.
Compared to a reference spectrum of the sun recorded with a resolution of $\lambda/\Delta\lambda = 500.000$, all features that must be visible at the lower resolution of BESO ($\lambda/\Delta\lambda = 50.000$) are identifiable. The entire spectral range defined in the optical design of the instrument is covered. This documents that the performance of the instrument is at the desired level.

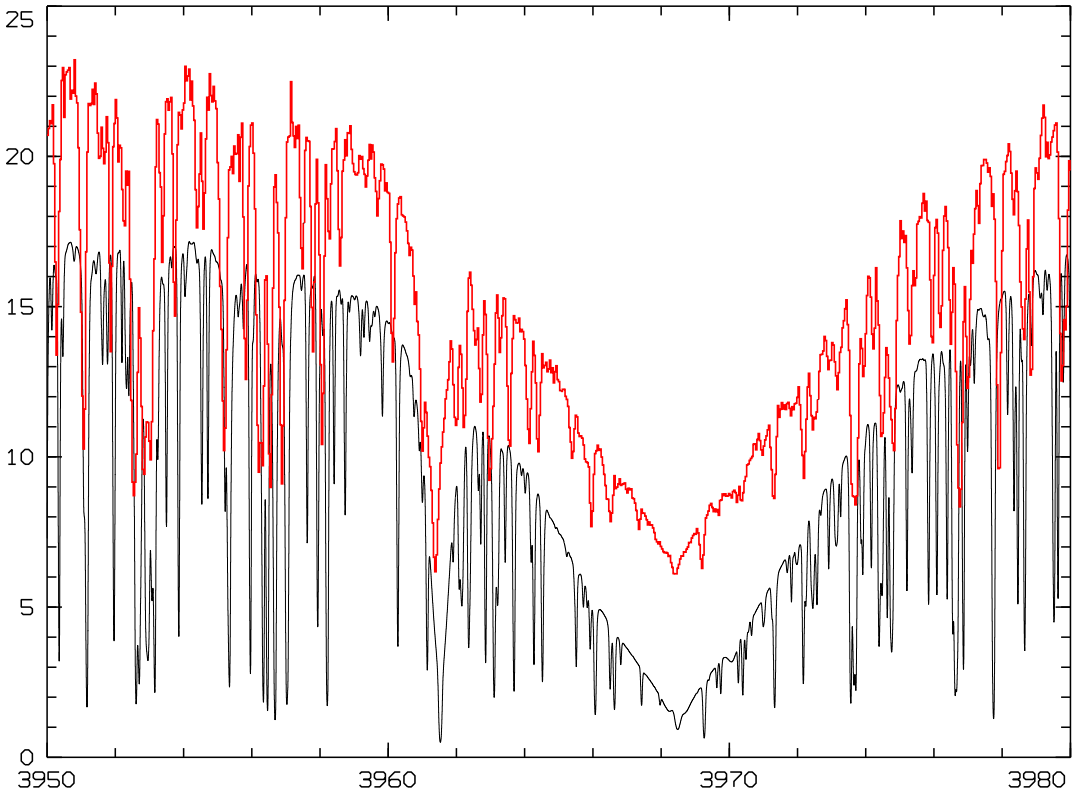

Figure 3.12: Section of solar spectrum with BESO (red, $\lambda/\Delta\lambda = 50.000$) compared to a reference spectrum with $\lambda/\Delta\lambda = 500.000$ (black). Spectral lines show all features that should be visible at the resolution of BESO. This data is not wavelength calibrated. The intensity axis has an arbitrary offset.

Chapter 4

BESO first light

After successful testing of the complete instrument in the laboratory BESO has been disassembled in October 2007. BESO reached the observatory in Chile by end of November 2007. During the transport the cold head of the closed cycle cooler for the CCD detector had been damaged and coolant was leaking from the high pressure tubing into the cryostat during operation.

The cold head has been brought back to Bochum to mend the broken coolant pipe. After repair and successful leakage testing, the cold head was re-installed at the observatory in February 2008. Unfortunately the repaired cold head did not provide sufficient cooling power to cool the detector down to its operating temperature of -100°C. A new cold head had to be manufactured which arrived at the observatory in August 2008.

During this unintended delay, the instrument had been set up at the observatory. The optics had been aligned up to final adjustments for which the working detector was required. The interface to the Hexapod-Telescope, the calibration unit and the instrument workstation had been installed and tested successfully.

The alignment of the fiber head has been tested at the telescope flange by projecting a laser through the fiber into the telescope optics. A tilt of the beam was not noticeable. The secondary mirror of the telescope was fully illuminated by the laser.

During the tests in the laboratory in Heidelberg it was verified, that the instrument reached the performance defined in the optical design. The spectral range from 370 nm to 860 nm is completely covered. The resolution on the detector was 2.2 pixels per spectral resolution element.

These tests have been repeated at the observatory confirming full spectral coverage. A detector resolution of 1.9 pixels per spectral resolution element could be achieved in the center of the detector plane. The final test data showed very low dark current of the detector and low noise of the readout electronics. After installing the stray light stops, very little internal reflections from within the instrument reached the detector, leading to improved contrast of the echellogram on the detector.

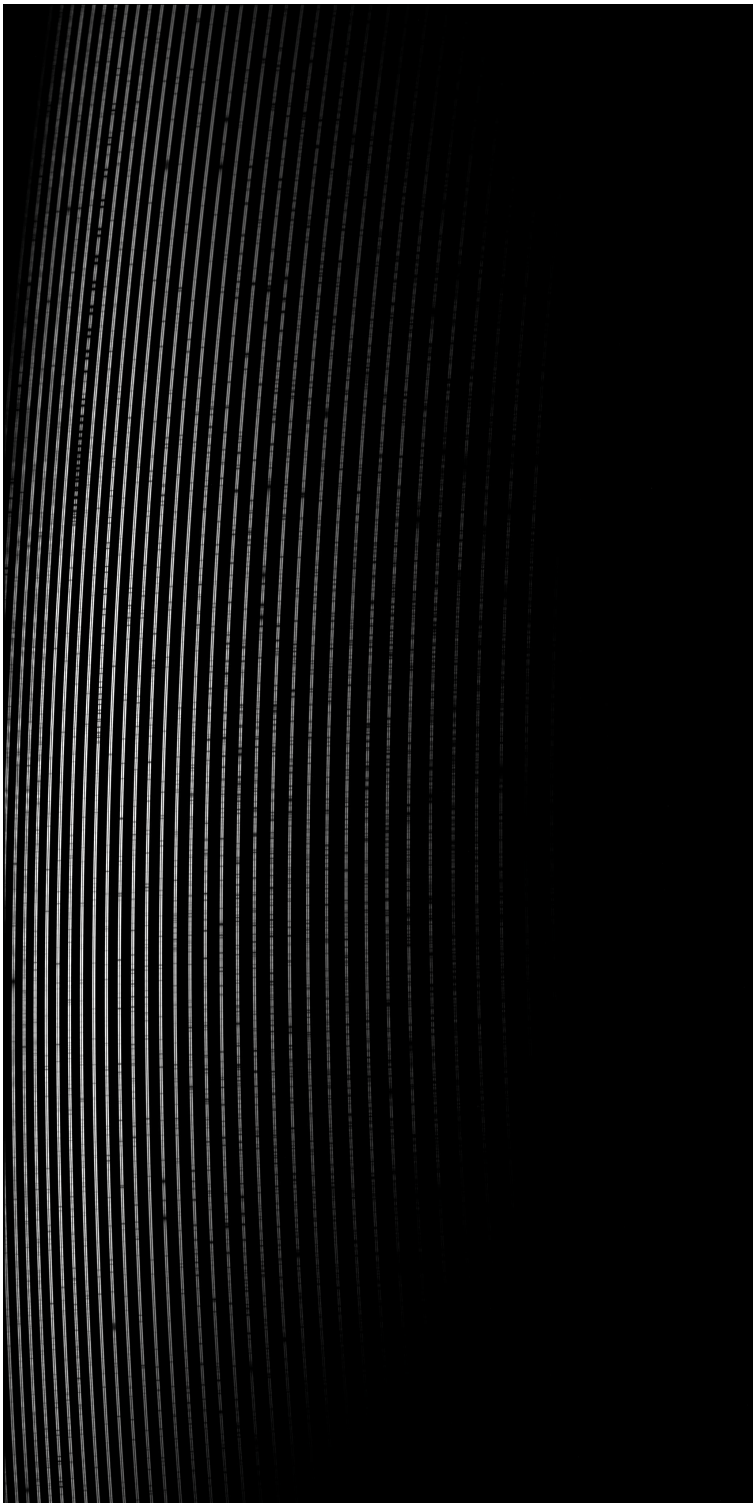

Figure 4.1: BESO first-light exposure observing Beta Ceti on August 30, 2008.

As first on-sky observation, the star Beta Ceti has been observed by Vera Hoffmeister on August 30, 2008 (Fig. 4.1). The spectrum has been extracted using the automatic data reduction pipeline.

The radial velocity of Beta Ceti has been measured on four spectral lines from the spectrum taken with BESO (Tab. 4.1 and Fig. 4.2). The measured average is 12.4±0.1 km/s. The star is a well documented radial velocity standard. The IAU reference velocity is 13.1±0.2 km/s, see e.g. Udry et al. (1999).

The deviation of 0.7 km/s of our measurement from the reference value corresponds to a wavelength offset of 0.0014 nm or 3.5 μm offset on the detector of the spectrograph.

The most likely reason for this offset is that the wavelength calibration data was taken during daytime and that the temperature stabilization of the instrument room was not in use for the first light observation, resulting in a temperature drift of a few degrees Celsius between the observation and the recording of the reference data. The thermal expansion coefficients of the main constituents of the instrument are $23 \cdot 10^{-6}$/K for aluminum and $13 \cdot 10^{-6}$/K for the steel bench. Regarding the dimensions of the instrument, the size of the optical bench is 2.5 x 1.5 m, it is obvious that the thermal expansion easily leads to shifts of several microns per Kelvin. Along the optical axis this shift is compensated by the temperature drift compensator, a Delrin rod that mechanical moves the camera to keep the optics in focus.

For science observations, several calibration frames taken before and after the observation will be averaged. The thermal stabilization limits the temperature drift of the instrument to ±0.1 K/h and ±0.5 K/day. This improves the absolute precision of the instrument for science observations. More precise radial velocity measurements can be obtained by fitting at set of spectral lines simultaneously.

Compared to a FEROS observation of the same object, recorded one year earlier with the 2.2 m telescope at La Silla, all features of the spectral lines are visible in the spectrum (Fig. 4.3). The profile of the absorption lines is identical. Only the superimposed noise of the instrument is different.

An absolute shift in wavelength is visible in the comparison (Fig. 4.4) that cannot be fully explained. The most likely explanation is that wavelength calibration files, used to extract the FEROS spectrum haven been taken on another day than the data. However, comparing the

Atom	Wavelength	Radial velocity
Na	588.9950 nm	12.9 ± 0.3 km/s
Na	589.5924 nm	11.6 ± 0.3 km/s
H	656.28516 nm	13.6 ± 0.3 km/s
K	769.8974 nm	11.56 ± 0.04 km/s
	Average	12.4 ± 0.1 km/s
	IAU Reference	13.1 ± 0.2 km/s

Table 4.1: Radial velocity measurement of the variable star Beta Ceti with BESO. The radial velocity has been determined by fitting a Gaussian to absorption lines. The deviation of the center of the Gaussian from the laboratory wavelength gives the radial velocity. The reference wavelengths have been taken from National Institute of Standards and Technology website.

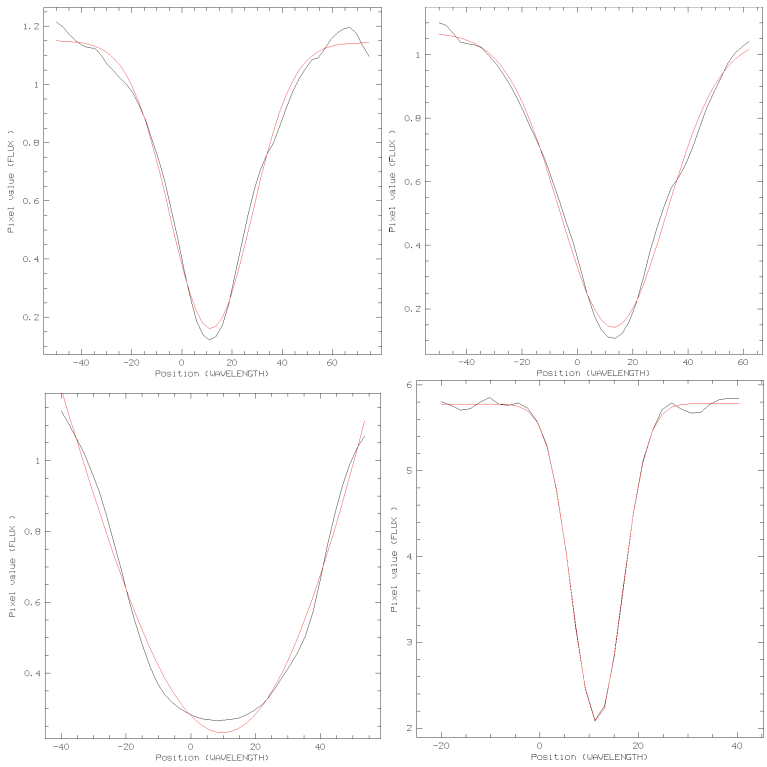

Figure 4.2: Fit of a Gaussian (red) to the spectrum (black) to determine the radial velocity. Na lines (top), H and K lines (bottom left and right).

Wavelength	FEROS	BESO
Na 588.9950 nm	-4.7 $\pm$ 0.3 km/s	12.9 $\pm$ 0.3 km/s
Na 589.5924 nm	-6.3 $\pm$ 0.3 km/s	11.6 $\pm$ 0.4 km/s
Difference	1.6 $\pm$ 0.2 km/s	1.4 $\pm$ 0.2 km/s

Table 4.2: Comparison of the radial velocity of Beta Ceti determined from two Na lines. The difference in velocity of both lines is the same with both instruments within the uncertainty of the measurement.

relative position of the two sodium lines in the spectrum shows that the relative measurement with both instruments agrees within the uncertainty of the fit to the spectral lines (Tab. 4.2).

The absolute wavelength calibration of the first light observation with BESO is close to the reference. The cause of the offset is understood and the calibration can be improved for future observations. The direct comparison of the spectrum recorded with BESO to a regular observation with FEROS shows that the desired resolution, spectral range and data quality of BESO has been achieved.
These results give confidence about the performance of the instrument.

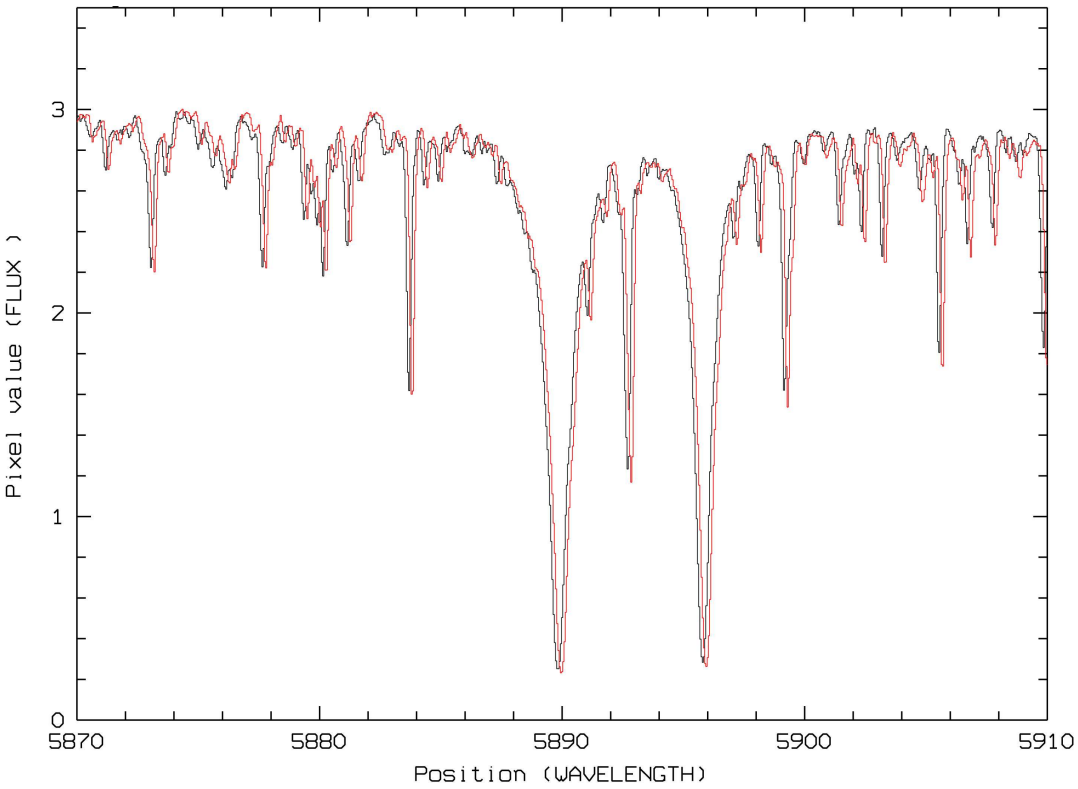

Figure 4.3: The plot shows a small section of two spectra of the variable star Beta Ceti. One spectrum has been recorded with FEROS on Aug. 27, 2007 (black line), the other with BESO on Aug. 29, 2008 (red line). The wavelength is given in Ångström and the flux in arbitrary units.

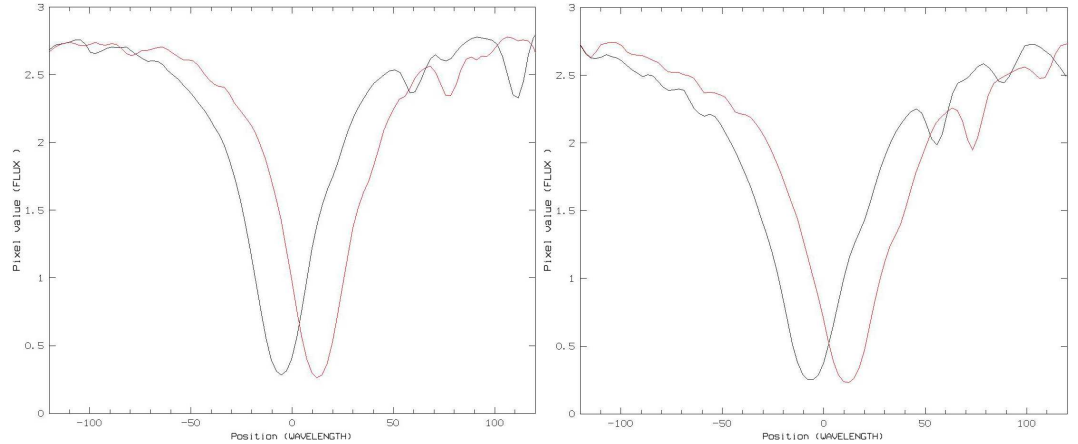

Figure 4.4: Detail of the Na lines at 588.995 nm and 589.592 nm. The plot shows radial velocity in km/s against flux in arbitrary units. According to fig. 4.3 the FEROS spectrum is plotted in black and the spectrum from BESO in red.

Chapter 5

Interstellar CH^+ absorption

The study of CH^+ absorption lines has become an important tool to measure the carbon isotope ratio in the interstellar medium.
^{12}C is produced in the triple-alpha fusion process of stars. Already the first stars in the universe, the population III stars, produced ^{12}C. Later star generations with higher initial metallicity produce ^{12}C and ^{13}C. The $^{12}C/^{13}C$ ratio is a tracer of the reprocessing of matter in stars and their evolution. The isotope ratio in the interstellar medium allows a measurement of the mass exchange between stars and the interstellar medium. The measurement of the carbon isotope ration can provide new insight into the evolution of stars and their interaction with the interstellar medium.
Two absorption lines of the CH^+ molecule at 423.2 nm and 395.7 nm are used to measure the interstellar carbon isotope ratio. If a molecule consists of a ^{13}C atom instead of the more abundant ^{12}C, the absorption lines shift slightly with the energy levels (-0.026 nm and +0.044 nm). The fact that the two lines are shifted in opposite directions in the spectrum makes the isotope measurement on CH^+ reliable, even if multiple absorbing clouds with different velocities appear on a line of sight towards a background star.
The environment in which CH^+ is formed is not completely understood. CH^+ is produced along reaction 5.1 from C.

$$C^+ + H_2 \rightarrow CH^+ + H \tag{5.1}$$

The reaction requires 0.398 eV of external energy or a temperature of 4650 K (Wilson and Rood, 1994). In an interstellar cloud velocities of few km/s are thought to be sufficient to power CH^+ production in a shock-front (Flower and Pineau des Forets, 1998). The photo-ionization of CH requires a photon of 13.25 eV.
The first isotope ratios measured on CH^+ showed a large scatter for different lines of sight. With better observations, the measurement on CH^+ is currently the best known method to determine the interstellar carbon isotope ratio. The results are in agreement with measurements retrieved from radio observations, see Centurion et al. (1995), Casassus et al. (2005), and Stahl et al. (2008).
This measurements relies on the assumption that no chemical fractionation or selective dissociation process changes the $^{12}CH^+/^{13}CH^+$ ratio from the local carbon isotope ratio. Chemical fractionation, where one isotope is energetically preferred over the other, has been

assumed by Watson (1976a). Such a process is known for the CO molecule, where reaction 5.2 frees 0.003 eV - equivalent to 35 K.

$$^{13}C^{+} + ^{12}CO \rightarrow ^{13}CO + ^{12}C^{+} \tag{5.2}$$

The measured deviation from the true isotope ratio depends exponentially on the temperature T_{kin} of the molecules (Wilson and Rood, 1994):

$$\left(\frac{^{13}CO}{^{12}CO}\right)_{measured} = \left(\frac{^{13}CO}{^{12}CO}\right)_{actual} \cdot exp\left(\frac{\Delta E}{kT_{kin}}\right) \tag{5.3}$$

Analog to the isotope exchange reaction 5.2, the production of $^{13}CH^{+}$ is favored over the production of $^{12}CH^{+}$ in an energetically low environment.
In the past decades several correlations of observable properties have been discussed to conclude on the environment in that CH^{+} is formed from CH. Typical observational samples consist of lines of sight close to each other in the direction of one association of stars or an open cluster. E.g. Crawford (1989b) used 9 lines of sight to study CH and CH^{+}, Gredel et al. (1993) used 20 lines of sight, Crane et al. (1995) also published a sample of 20 lines of sight and Gredel (1997) used 19 lines of sight. Fig. 5.1, 5.2 and 5.3 show typical datasets that have been used to find a correlation between column density and extinction.
Intensive observations have been carried out in the direction of ζ Ophiuchi, indicating for the first time that CH and CH^{+} exist in regions of different character, see Lambert et al. (1990) and Crawford et al. (1994).
The isotopes of the CH^{+} molecule and their energy levels have also been studied in laboratory experiments (Pearson and Drouin, 2006).
To make the isotope ratio measured on CH^{+} more credible it is necessary to research the environment in that CH^{+} is formed. In the following sections, the absorption lines of the rare and chemically unstable CH^{+} are compared with absorption lines of the CH molecule that is stable and abundant. From these measurements, it is possible to conclude on the environment in which the two molecules reside and the extent of chemical fractionation of CH^{+} in the interstellar medium.

5.1 Data

To investigate the environment in which CH^{+} is formed with a substantial sample, 198 high resolution spectra are used. They were obtained during two observing campaigns in 2006 and 2008 with FEROS at the La Silla observatory by Otmar Stahl. 334 spectra from the FEROS archive enlarge the sample. All stars in the sample are of spectral type O or B because these early type stars show a smooth spectrum without too many lines that could interfere with the absorption lines of the interstellar medium.
The 532 spectra have been classified. 240 of them have been used, taken from 108 lines of sight to background stars where CH and CH^{+} absorption appears at only one velocity and where the absorption lines could be fitted with a single Gaussian. Two lines of the $^{12}CH^{+}$ molecule (423.254 nm and 395.77 nm) and one line of the CH molecule at 430.031 nm from each spectrum form the dataset for this research.

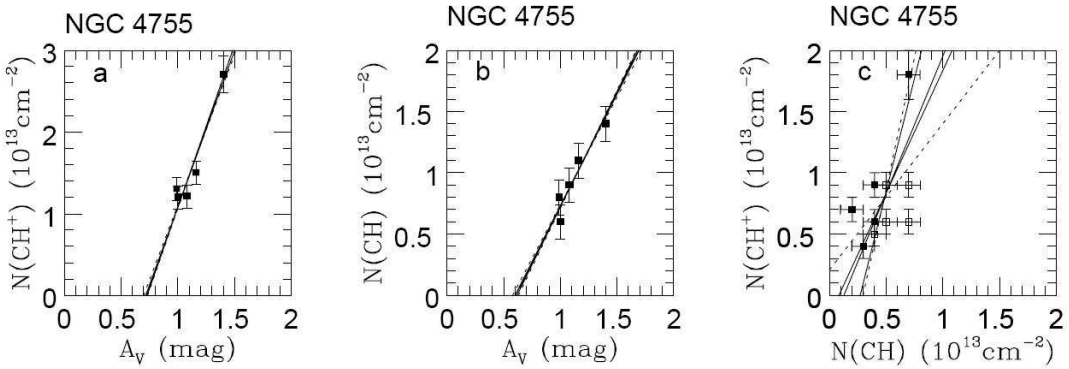

Figure 5.1: Measurement of CH^+ (left) and CH (center) column densities over visual extinction. Right: CH^+ over CH column density. Each point represents one line of sight towards a member of the open cluster NGC 4755. From Gredel (1997).

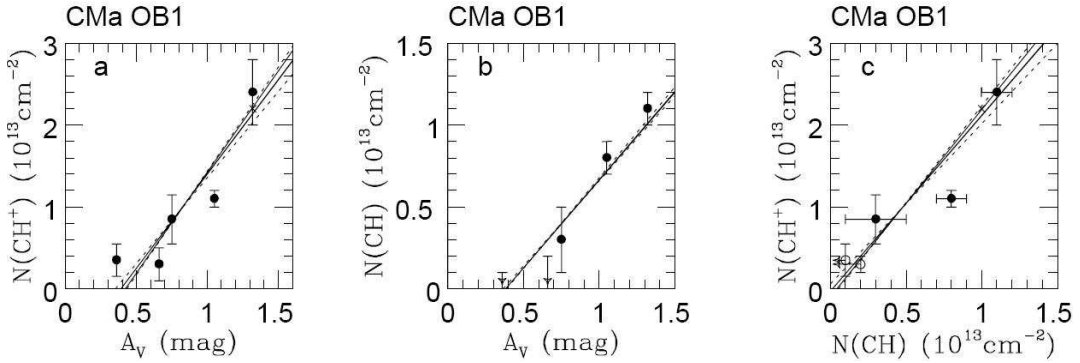

Figure 5.2: Measurement of CH^+ (left) and CH (center) column densities over visual extinction. Right: CH^+ over CH column density. Each point represents one line of sight towards a member of the association of stars CMa OB 1. From Gredel (1997).

The baseline of each spectrum is fitted with a first order polynomial and the absorption line with a single Gaussian. The shift of the center of the Gaussian with respect to the laboratory wavelength of the line is interpreted as velocity of the absorbing cloud. The equivalent width EW of the line is computed by

$$EW = \frac{\lambda \cdot 1.06447}{c} G_{depth} G_{FWHM} \tag{5.4}$$

where λ is the rest wavelength of the absorption line, c the speed of light, G_{depth} the depth of the Gaussian fitted to the line and G_{FWMH} the full width half maximum of the Gaussian. To calculate the intrinsic width s_{intr} of the line, the instrumental line profile, a Gaussian with a width of 6 km/s, has been subtracted from the width derived from the fit:

$$s_{intr} = \sqrt{G_{FWMH}^2 - \left(\frac{c \cdot \Delta\lambda}{\lambda}\right)^2} \tag{5.5}$$

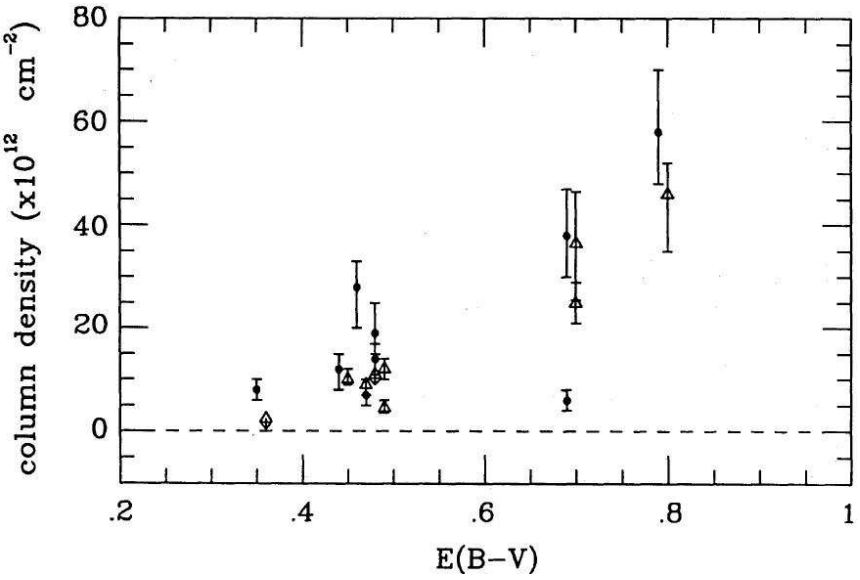

Figure 5.3: Measurement of CH^+ (dots) and CH (triangles) column densities over the B-V reddening. Each point represents one line of sight towards a member of the association of stars Sco OB 1. From Crawford (1989b).

The complete dataset and the derived measurements are listed at the end of this chapter (Tab. 5.2).

The fit uncertainties are used to estimate the uncertainties of the measured properties. The typical fit quality can be seen in Fig. 5.4 and Fig. 5.5. For lines of sight with multiple observations, the individual fit results have been averaged to one data point.

The equivalent line width measured in several observations towards the same object is shown as example in Fig. 5.6. A systematic offset between our own observations and the data from the archive could not be found. Some observations from the archive have a rather low signal-to-noise quality resulting in larger error bars of the data point. The uncertainties derived from the fit match the variation of the values. The values are distributed randomly.

The acquired dataset was compared to measurements published earlier by Megier et al. (2005) and Weselak et al. (2008). A comparison of the derived equivalent widths for all objects that are in this dataset and at least one of the other two, is shown in table 5.1. Fig. 5.7 shows the comparison and a linear fit, that deviates only within its uncertainty from unity where all observations show the same value.

These tests give confidence about the quality of the dataset and the correctness of the line fitting procedure. The observed lines of sight are spread across the Milky Way as can be seen in fig. 5.8. The dataset is expected to be a representative sample for the study of the environment in that CH^+ forms, because it covers lines of sight with different lengths, to various directions in the Milky Way and covers several magnitudes of extinction.

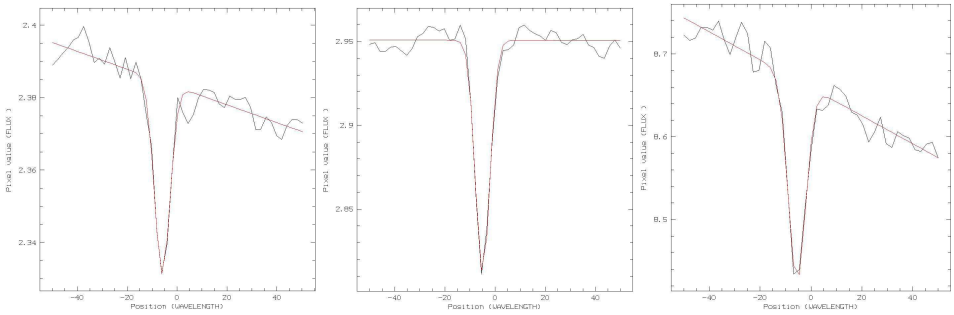

Figure 5.4: Fit of a single Gaussian to the CH_{430}, CH^{+}_{423} and CH^{+}_{395} (from left to right) absorption line in the direction of HD 147165.

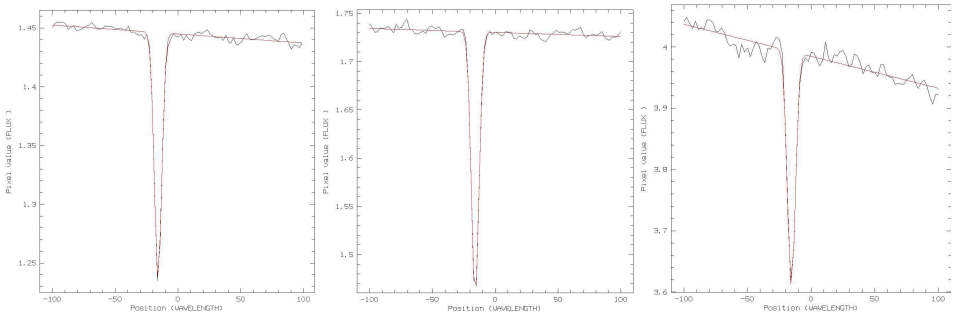

Figure 5.5: Fit of a single Gaussian to the CH_{430}, CH^{+}_{423} and CH^{+}_{395} (from left to right) absorption line in the direction of HD 154445.

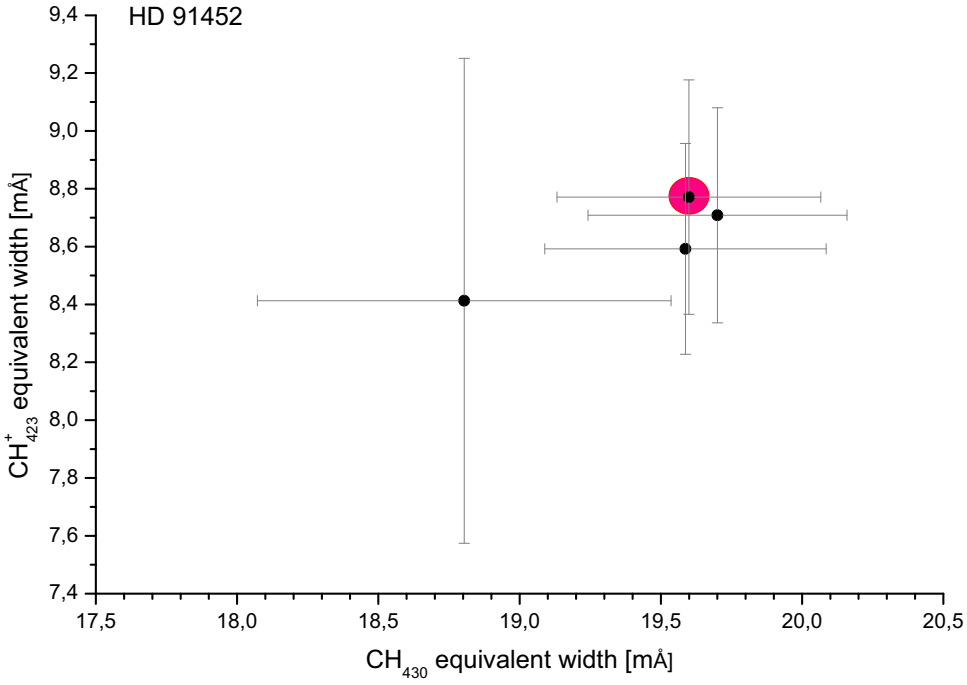

Figure 5.6: Four measurements of equivalent line widths in the direction of HD 91452. The measurement marked with a red dot originates from the observations in 2006, and lies well within the range of the other three observations from the FEROS archive.

	CH equivalent width [mÅ]		
Object	own	Weselak	Megier
HD46149	17.2 ± 0.7	–	18.1 ± 0.9
HD46150	10.5 ± 0.8	12.1 ± 0.7	–
HD46223	17.2 ± 0.6	18.6 ± 1.0	–
HD46573	31.0 ± 1.2	28.1 ± 1.7	–
HD47432	9.9 ± 0.7	9.7 ± 0.5	–
HD92964	10.9 ± 0.5	–	10.4 ± 0.2
HD106343	4.2 ± 0.4	–	4.1 ± 0.2
HD147165	2.6 ± 0.3	2.9 ± 0.1	–
HD147889	50.2 ± 0.9	50.2 ± 1.7	–
HD148688	12.6 ± 0.7	14.2 ± 0.6	14.8 ± 0.3
HD149038	8.9 ± 0.5	–	9.1 ± 0.3
HD151804	4.5 ± 0.7	–	6.4 ± 0.3
HD152219	9.2 ± 0.8	10.7 ± 0.5	–
HD152233	12.0 ± 0.6	13.1 ± 0.1	–
HD152234	9.4 ± 0.9	12.8 ± 0.3	–
HD152246	13.2 ± 0.9	14.7 ± 0.5	–
HD152249	7.6 ± 0.9	11.5 ± 0.2	–
HD152314	12.1 ± 0.9	16.2 ± 0.5	–
HD152667	14.4 ± 0.7	15.4 ± 0.5	–
HD154090	21.7 ± 0.8	22.6 ± 0.8	22.9 ± 0.4
HD154445	15.3 ± 0.3	15.5 ± 0.4	15.0 ± 0.3

Table 5.1: Comparison of the equivalent width measured in this dataset and data published in Megier et al. (2005) and Weselak et al. (2008). For a graphical visualization see fig. 5.7.

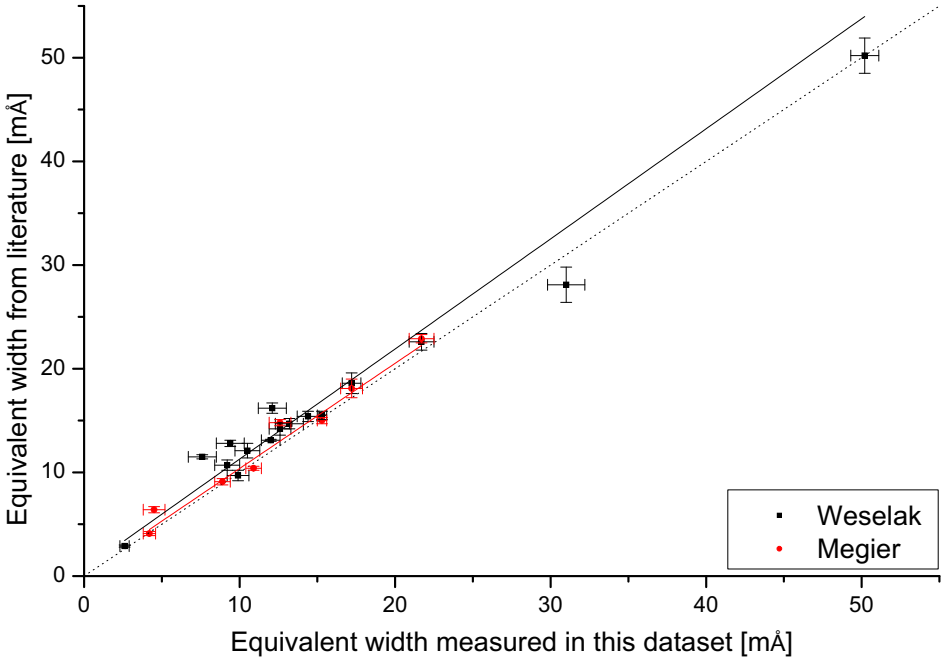

Figure 5.7: The graph shows the equivalent width of CH derived from this dataset compared against the data published by Megier et al. (2005) (red) and Weselak et al. (2008) (black). The dotted black line denotes unity. The continuous lines are linear fits to the data sets, showing deviation from the reference line only within the uncertainty of the fit (1.01 ± 0.08 for Megier against this dataset and 1.06 ± 0.06 for Weselak's against this).

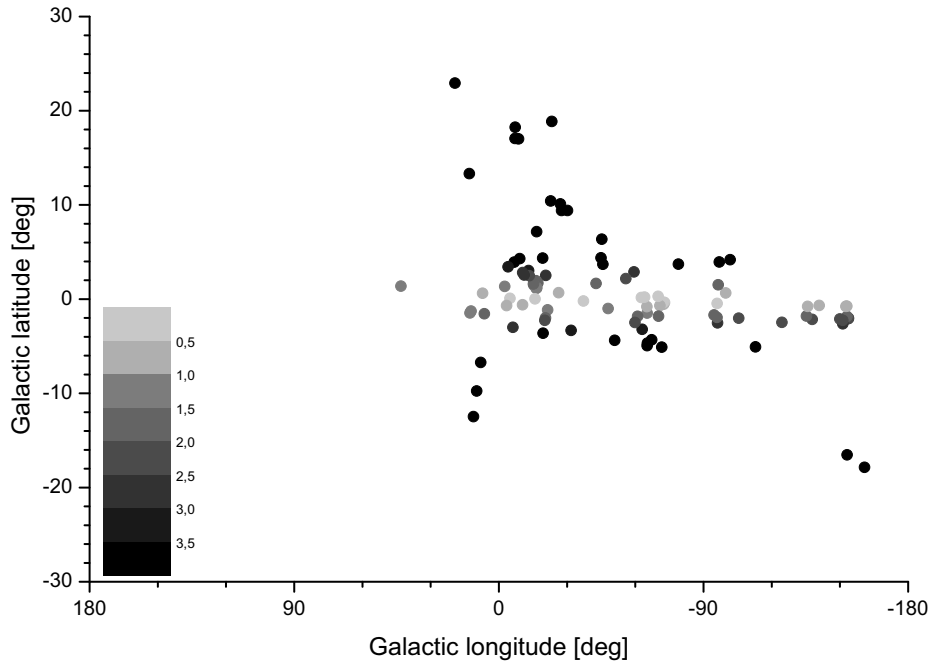

Figure 5.8: Distribution of the objects in this dataset in galactic coordinates (center of Milky Way is the center of the graph). The color of each object shows the extinction to the background object.

	Velocity [km/s]			Equivalent width [mÅ]			Intrinsic width [km/s]	
Object	CH_{430nm}	CH^{+}_{423nm}	CH^{+}_{395nm}	CH_{430nm}	CH^{+}_{423nm}	CH^{+}_{395nm}	CH_{430nm}	CH^{+}_{423nm}
HD101190	8.2±0.3	6.8±0.2	7.6±0.5	6.0±0.7	7.7±0.7	3.6±0.8	3.1± 2.2	4.9±1.6
HD101545	8.7±0.4	9.6±0.2	9.4±0.5	4.0±0.8	7.9±0.8	4.5±0.8	2.2± 2.9	3.8±1.9
HD102997	10.1±0.4	11.4±0.2	10.4±0.3	2.1±0.4	8.3±0.6	4.4±0.4	1.6± 3.8	7.0±1.3
HD103270	6.4±0.4	5.4±0.2	5.6±0.5	6.0±1.0	16.5±1.0	8.3±1.6	3.6± 1.9	5.4±1.5
HD104631	7.6±0.3	7.8±0.2	8.3±0.5	4.8±0.7	11.7±0.9	6.3±1.1	2.8± 2.4	4.4±1.7
HD106343	7.5±0.2	7.3±0.1	5.4±0.2	4.2±0.4	16.4±0.4	9.3±0.6	3.7± 1.9	4.4±1.7
HD108002	9.2±0.3	7.9±0.2	6.0±0.5	5.7±0.6	8.8±0.7	5.7±0.8	6.6± 1.4	7.2±1.3
HD109091	6.4±0.5	6.7±0.2	7.2±0.4	4.8±1.0	12.3±0.8	6.5±1.1	4.8± 1.6	4.8±1.6
HD112999	6.8±0.6	5.8±0.2	6.7±0.7	2.9±0.8	12.0±0.8	5.7±1.4	–	6.6±1.4
HD120680	-5.0±0.4	-3.9±0.2	-4.8±0.5	4.8±0.7	14.4±1.0	5.7±1.0	6.0± 1.4	9.8±1.2
HD123590	2.0±0.3	3.3±0.3	2.9±0.4	3.6±0.7	8.6±1.2	5.2±0.9	–	4.4±1.7
HD124195	5.0±0.2	6.5±0.1	6.7±0.1	8.0±0.7	12.9±0.4	7.6±0.5	4.4± 1.7	3.8±1.9
HD124620	0.6±0.1	3.5±0.2	2.2±0.4	10.6±0.7	8.0±0.6	4.5±0.6	3.4± 2.0	7.1±1.3
HD125288	2.1±0.1	1.7±0.2	0.2±0.1	6.4±0.4	12.6±1.1	9.4±0.5	4.1± 1.8	1.8±3.5
HD129090	2.2±0.3	1.9±0.1	2.3±0.2	6.7±0.8	19.8±0.9	11.7±1.0	4.3± 1.7	4.3±1.7
HD136899	3.9±0.1	1.3±0.4	0.0±0.8	10.1±0.6	4.7±0.8	4.5±1.2	3.4± 2.0	2.1±3.0
HD137518	1.0±0.4	0.8±0.4	-1.2±0.7	1.9±0.8	7.6±1.1	4.8±1.4	–	6.5±1.4
HD137595	-0.3±0.2	-0.8±0.1	-0.5±0.3	7.9±0.6	12.9±0.7	7.1±0.8	6.0± 1.4	6.0±1.4
HD139431	0.5±0.6	-0.3±0.2	0.5±0.6	3.2±0.8	9.1±0.7	5.3±1.1	4.5± 1.7	4.1±1.8
HD139432	1.6±0.4	2.4±0.2	1.1±0.2	3.5±0.7	19.2±1.2	10.9±0.9	3.4± 2.0	5.6±1.5
HD142448	4.0±0.1	3.2±0.2	3.1±0.2	13.0±0.5	14.2±0.9	7.6±0.6	4.3± 1.7	7.1±1.3
HD144858	4.7±1.0	1.9±0.3	2.2±0.7	1.1±0.6	3.5±0.6	1.5±0.6	–	3.1±2.2
HD146444	-6.0±0.6	-6.7±0.4	-6.6±0.7	2.9±0.8	9.8±1.1	5.5±1.3	3.0± 2.2	8.7±1.2
HD147165	-5.7±0.2	-5.6±0.1	-5.9±0.3	2.6±0.3	4.5±0.3	2.8±0.4	3.9± 1.9	2.2±2.9
HD147196	-6.6±0.1	-6.1±0.2	-6.6±0.4	13.9±0.5	4.6±0.5	3.0±0.6	3.1± 2.2	3.3±2.1
HD147889	-6.9±0.0	-7.9±0.1	-8.7±0.2	50.2±0.9	26.3±0.8	15.9±1.1	3.1± 2.2	3.8±1.9
HD148546	-1.7±0.1	-0.9±0.1	-2.6±0.2	15.2±0.6	24.1±0.8	14.5±1.0	6.1± 1.4	5.6±1.5

	Velocity [km/s]			Equivalent width [mÅ]			Intrinsic width [km/s]	
Object	CH_{430nm}	CH^{+}_{423nm}	CH^{+}_{395nm}	CH_{430nm}	CH^{+}_{423nm}	CH^{+}_{395nm}	CH_{430nm}	CH^{+}_{423nm}
HD148688	-1.2±0.2	-1.5±0.1	-1.1±0.1	12.6±0.7	22.9±0.5	13.0±0.7	6.4± 1.4	5.6±1.5
HD149038	-2.3±0.2	-2.9±0.0	-2.6±0.1	8.9±0.5	26.9±0.4	15.8±0.4	8.0± 1.3	5.7±1.5
HD150958	-17.4±0.3	-17.5±0.1	-17.2±0.2	8.6±0.9	18.2±1.1	10.9±1.1	3.4± 2.0	4.1±1.8
HD151515	-4.5±0.4	-2.8±0.1	-2.6±0.5	6.3±0.7	23.7±0.7	12.2±1.6	10.8± 1.1	9.7±1.2
HD151804	-1.7±0.7	-5.1±0.1	-4.8±0.1	4.5±0.7	8.9±0.3	5.6±0.3	12.0± 1.1	5.9±1.4
HD152149	-1.5±0.1	-2.3±0.2	-2.3±0.5	12.7±0.8	11.3±0.9	4.8±1.1	4.1± 1.8	6.9±1.3
HD152219	-0.5±0.3	-3.4±0.2	-3.2±0.5	9.2±0.8	22.3±1.0	11.8±1.2	8.6± 1.2	13.9±1.1
HD152233	1.7±0.2	-0.7±0.2	-0.6±0.3	12.0±0.6	22.4±0.9	12.7±1.0	6.8± 1.3	12.1±1.1
HD152234	1.1±0.3	0.8±0.2	1.1±0.3	9.4±0.9	19.7±1.2	11.0±1.0	6.8± 1.3	9.7±1.2
HD152246	1.4±0.2	-2.2±0.1	-2.1±0.3	13.2±0.9	12.4±0.6	6.9±0.6	6.7± 1.3	7.1±1.3
HD152247	1.8±0.1	1.1±0.2	1.4±0.3	15.7±0.7	13.7±0.8	7.1±0.8	4.6± 1.7	8.6±1.2
HD152249	1.0±0.3	-0.6±0.3	-0.3±0.4	7.6±0.9	16.1±1.1	9.4±1.2	5.8± 1.4	10.4±1.2
HD152314	1.3±0.2	0.7±0.3	1.1±0.3	12.1±0.9	15.6±1.2	8.8±0.9	5.1± 1.6	8.3±1.2
HD152405	-9.2±0.5	-8.3±0.5	-8.0±0.7	6.3±0.8	14.5±1.3	8.2±1.2	10.9± 1.1	15.6±1.1
HD152541	0.2±0.5	-0.2±0.2	-0.7±0.4	5.0±1.0	10.5±0.9	7.4±1.2	5.1± 1.5	4.2±1.7
HD152667	-1.0±0.2	-2.5±0.2	-2.6±0.5	14.4±0.7	11.3±0.7	5.7±0.9	6.9± 1.3	8.4±1.2
HD152723	1.7±0.3	1.1±0.3	0.3±0.6	7.5±0.8	10.8±0.9	5.1±1.0	5.3± 1.5	9.5±1.2
HD152901	-3.7±0.4	-3.4±0.1	-3.8±0.3	8.8±1.0	28.2±1.0	16.2±1.2	7.4± 1.3	9.3±1.2
HD153102	-0.8±0.4	-2.3±0.1	-2.4±0.4	6.4±1.0	14.7±0.7	8.6±1.0	7.4± 1.3	5.4±1.5
HD153382	-0.3±0.1	-1.0±0.2	-1.3±0.5	12.3±0.6	7.3±0.6	3.8±0.7	3.6± 2.0	6.1±1.4
HD154043	-11.5±0.1	-6.0±0.3	-5.2±0.6	23.7±1.0	24.0±1.3	14.2±1.6	8.6± 1.2	16.4±1.1
HD154090	-3.1±0.1	-2.4±0.1	-3.8±0.2	21.7±0.8	18.3±0.6	9.7±0.7	5.6± 1.5	8.5±1.2
HD154218	-3.5±0.3	-5.5±0.3	-4.6±0.5	5.8±0.7	7.3±0.8	3.3±0.7	3.8± 1.9	6.9±1.3
HD154385	-3.3±0.1	-3.6±0.1	-3.7±0.2	26.4±0.7	28.0±1.0	17.2±1.1	4.3± 1.7	6.3±1.4
HD154445	-15.9±0.0	-15.9±0.0	-15.5±0.1	15.3±0.3	17.0±0.2	9.8±0.4	3.5± 2.0	4.0±1.8
HD155450	-2.5±0.1	-1.2±0.1	-0.9±0.2	7.0±0.3	8.3±0.3	4.1±0.4	6.1± 1.4	4.9±1.6
HD156688	-2.5±0.2	-4.0±0.2	-4.0±0.6	7.1±0.6	7.2±0.5	3.7±0.8	6.4± 1.4	5.2±1.5

	Velocity [km/s]			Equivalent width [mÅ]			Intrinsic width [km/s]	
Object	CH_{430nm}	CH^{+}_{423nm}	CH^{+}_{395nm}	CH_{430nm}	CH^{+}_{423nm}	CH^{+}_{395nm}	CH_{430nm}	CH^{+}_{423nm}
HD157016	-3.9±0.8	-3.5±0.1	-3.0±0.2	3.5±0.9	10.3±0.5	5.2±0.5	6.5±-1.4	4.0±1.8
HD157857	-14.3±0.3	-13.1±0.1	-13.2±0.3	9.0±0.9	22.6±0.9	13.5±1.5	8.1± 1.3	6.9±1.3
HD158859	-2.1±0.1	-2.3±0.1	-1.9±0.2	16.7±0.7	13.6±0.6	7.8±0.8	4.5± 1.7	5.7±1.5
HD159090	-2.7±0.2	-3.2±0.1	-2.9±0.2	8.0±0.7	20.8±0.8	13.8±1.0	4.1± 1.8	6.2±1.4
HD160202	-5.8±0.7	-0.8±0.2	-0.7±0.4	4.0±0.7	6.7±0.5	4.3±0.6	8.8± 1.2	6.5±1.4
HD160575	-2.4±0.2	-4.6±0.2	-4.5±0.5	15.3±0.9	26.9±1.1	15.8±1.5	9.2± 1.2	12.1±1.1
HD163892	-5.3±0.1	-6.1±0.1	-4.9±0.2	15.8±0.6	15.9±0.6	7.5±1.0	2.7± 2.5	5.0±1.6
HD165246	-4.7±0.4	-4.3±0.2	-5.5±0.5	4.8±0.8	9.8±0.9	4.2±1.0	4.5± 1.7	4.8±1.6
HD167659	-8.7±0.2	-8.9±0.2	-8.8±0.2	6.5±0.7	17.6±1.3	9.8±0.9	0.9± 6.5	4.5±1.7
HD168021	-7.7±0.2	-8.1±0.1	-7.8±0.2	9.4±0.5	19.4±0.6	10.2±0.8	6.2± 1.4	7.2±1.3
HD170235	-3.5±0.3	-4.8±0.3	-3.4±0.9	6.3±0.7	6.4±0.6	3.0±0.9	7.9± 1.3	7.9±1.3
HD173117	-5.4±0.2	-4.6±0.1	-4.4±0.2	8.9±0.6	13.6±0.5	7.7±0.4	7.2± 1.3	6.1±1.4
HD175852	-10.0±0.4	-7.6±0.2	-9.4±0.2	3.0±0.6	17.2±1.0	8.0±0.7	1.8± 3.6	6.5±1.4
HD177624	-12.5±0.2	-13.3±0.3	-13.1±0.5	11.4±0.8	11.1±0.9	5.3±1.0	6.4± 1.4	7.3±1.3
HD35149	22.9±0.2	23.1±0.1	23.4±0.2	4.5±0.4	10.3±0.3	4.5±0.4	5.3± 1.5	4.9±1.6
HD37903	27.5±0.2	27.1±0.1	27.1±0.3	7.0±0.5	10.3±0.5	5.3±0.7	3.3± 2.1	2.8±2.4
HD46149	25.5±0.2	25.0±0.1	25.5±0.3	17.2±0.7	19.3±0.8	10.3±1.0	9.5± 1.2	9.4±1.2
HD46150	24.8±0.3	26.3±0.2	26.8±0.5	10.5±0.8	12.3±0.6	5.8±0.9	8.8± 1.2	9.7±1.2
HD46202	24.5±0.2	24.5±0.3	24.5±0.5	14.1±1.0	15.4±1.4	8.4±1.3	6.3± 1.4	8.7±1.2
HD46223	26.6±0.1	26.7±0.1	26.8±0.2	17.2±0.6	20.7±1.0	13.5±0.9	7.8± 1.3	6.1±1.4
HD46485	26.4±0.1	25.6±0.2	26.0±0.3	22.7±0.9	24.2±1.5	12.8±1.2	6.9± 1.3	8.5±1.2
HD46573	26.7±0.1	28.8±0.1	28.2±0.3	31.0±1.2	24.5±0.8	15.2±1.4	10.0± 1.2	7.6±1.3
HD46847	28.1±0.2	28.3±0.1	28.5±0.3	28.1±1.8	35.1±1.5	23.6±2.6	5.7± 1.5	5.1±1.5
HD47240	26.1±0.3	26.4±0.2	26.4±0.2	6.3±0.7	17.4±0.9	9.6±0.6	9.1± 1.2	7.8±1.3
HD47382	25.7±0.2	24.8±0.2	25.0±0.4	10.8±0.7	13.2±0.6	7.3±0.7	9.0± 1.2	7.6±1.3
HD47432	24.6±0.3	25.6±0.4	25.1±0.6	9.9±0.7	8.6±0.7	4.6±0.7	8.8± 1.2	10.7±1.2
HD52266	32.5±0.4	32.2±0.1	32.4±0.2	5.7±0.7	11.6±0.5	5.7±0.5	9.6± 1.2	6.0±1.4

	Velocity [km/s]			Equivalent width [mÅ]			Intrinsic width [km/s]	
Object	CH_{430nm}	CH^{+}_{423nm}	CH^{+}_{395nm}	CH_{430nm}	CH^{+}_{423nm}	CH^{+}_{395nm}	CH_{430nm}	CH^{+}_{423nm}
HD52382	35.0±0.2	36.9±0.1	35.2±0.2	7.3±0.5	18.9±0.5	10.2±0.7	5.5± 1.5	5.1±1.6
HD53974	32.2±0.3	32.0±0.1	30.1±0.2	5.4±0.5	12.4±0.3	6.3±0.5	9.5± 1.2	5.0±1.6
HD54662	35.1±0.3	35.4±0.1	34.6±0.2	6.5±0.7	9.9±0.4	5.3±0.5	4.9± 1.6	4.5±1.7
HD58510	45.5±0.4	46.5±0.1	46.7±0.3	4.3±0.7	11.0±0.5	5.9±0.8	5.4± 1.5	5.1±1.5
HD61827	38.4±0.1	39.2±0.2	38.3±0.3	32.9±0.8	12.3±1.1	6.8±0.9	9.0± 1.2	5.9±1.4
HD68450	31.9±0.8	26.7±0.2	27.0±0.3	5.8±0.7	7.2±0.5	4.5±0.5	17.8± 1.1	6.3±1.4
HD73568	16.2±0.1	17.5±0.2	17.9±0.5	19.4±0.9	16.5±0.9	9.4±1.5	4.4± 1.7	7.9±1.3
HD73882	21.9±0.1	21.9±0.1	22.4±0.1	24.5±0.5	18.2±0.5	9.3±0.5	3.6± 2.0	6.2±1.4
HD74194	21.9±0.2	20.2±0.1	20.7±0.3	11.7±0.7	16.5±0.6	8.7±0.8	9.4± 1.2	10.3±1.2
HD75149	22.0±0.1	23.5±0.2	22.2±0.2	14.9±0.6	9.2±0.6	5.4±0.4	8.3± 1.2	5.4±1.5
HD75211	20.3±0.1	23.3±0.1	23.6±0.1	18.8±0.8	26.0±0.7	14.9±0.8	8.5± 1.2	4.8±1.6
HD75222	24.4±0.2	29.2±0.1	29.4±0.2	29.4±1.0	36.6±1.3	21.1±1.0	13.4± 1.1	9.5±1.2
HD76341	21.1±0.1	20.8±0.0	21.0±0.1	26.5±0.5	38.7±0.4	22.9±0.5	5.1± 1.5	4.8±1.6
HD77581	24.2±0.1	24.6±0.3	24.5±0.6	26.4±1.3	26.5±1.7	16.2±2.3	6.3± 1.4	12.2±1.1
HD89767	8.7±0.3	10.5±0.1	10.4±0.3	8.6±0.8	20.5±0.7	11.4±1.0	5.5± 1.5	7.8±1.3
HD91452	9.0±0.1	8.8±0.1	9.0±0.4	19.4±0.6	8.6±0.5	5.1±0.8	3.4± 2.0	3.3±2.1
HD92964	7.2±0.2	6.7±0.1	5.1±0.3	10.9±0.5	8.2±0.4	4.4±0.5	8.0± 1.3	5.7±1.5
HD93250	6.4±0.4	6.4±0.3	6.5±0.7	4.0±0.6	5.4±0.6	2.4±0.7	5.3± 1.5	7.2±1.3
HD93403	4.9±0.1	4.6±0.3	3.9±0.7	12.9±0.7	7.0±0.6	4.2±0.8	5.5± 1.5	7.9±1.3
HD94910	17.7±0.1	16.7±0.1	16.9±0.2	45.6±1.0	51.8±1.3	34.2±2.0	6.5± 1.4	6.8±1.3
HD94963	9.9±0.3	10.3±0.1	10.1±0.4	3.2±0.4	6.0±0.3	2.9±0.6	4.0± 1.8	3.2±2.1
HD96248	0.9±0.2	0.5±0.2	1.1±0.4	12.2±0.7	16.4±0.7	8.5±0.9	9.3± 1.2	10.6±1.2
HD97522	7.0±0.1	6.7±0.1	7.0±0.2	17.8±0.7	16.6±0.7	9.9±0.9	3.2± 2.1	4.6±1.6
HD99785	7.3±0.2	6.4±0.2	6.8±0.6	7.4±0.7	8.9±0.7	3.6±1.0	3.5± 2.0	6.2±1.4
HD99857	6.8±0.3	6.3±0.2	6.1±0.6	5.1±0.6	6.1±0.5	2.8±0.7	6.2± 1.4	5.4±1.5
NGC2546-0682	32.6±0.9	26.9±0.2	26.5±0.3	4.8±0.8	7.4±0.5	3.7±0.5	15.0± 1.1	6.6±1.4

Table 5.2: For 108 lines of sight three absorption lines have been fitted with a single Gaussian. The first column denotes the background object. The measured velocity is the shift of the center of the absorption line from the laboratory value. The intrinsic width is the measured line width corrected for the instrumental line profile.

5.2 Results

In the following section, several correlations are presented, which are formed of observable properties of the absorption lines in the dataset. These correlations are used to characterize the physical processes in the interstellar medium.

To quantify the significance of a correlation, the adjusted R^2 value is used as coefficient of determination. After calculating a linear regression to a dataset by minimizing χ^2, one can obtain the R^2_{adj} using eq. 5.6.

$$R^2_{adj} = \frac{\sum_i \Delta y_i^2/(n-2)}{\sum_i y_i^2/(n-1)} \tag{5.6}$$

In the numerator, the deviation from the fitted line Δy is summed up for all data points (residual sum of squares) and divided by the number of data points n minus two to adjust the coefficient of determination to the degrees of freedom of the dataset. In the denominator the total sum of squares is divided by $n-1$.

The interpretation of the R^2_{adj} is that it gives the percentage of the variation in a dataset that is accounted for by the linear model used to fit the dataset.

Correlations between the CH line and CH^+_{423} line at 423 nm in the dataset will be tested. To relate these scientifically interesting correlations to a known correlation in the dataset, the CH^+_{423} line and the CH^+_{395} line will be compared. This will help to interpret the correlations in this observational dataset.

5.2.1 Velocities

The motion of the absorbing matter with respect to the earth shifts the absorption lines from their laboratory values. Different velocities of absorbing clouds indicate different positions on the line of sight.

The heliocentric motion of the earth has been deducted during the reduction of the spectra. Due to the motion of the sun in the Milky Way, the relative velocity v(CH^+_{423}) - v(CH) has to be used.

The mean of the velocity distribution of v(CH^+_{423}) - v(CH) is not significantly different from zero (Fig. 5.9). As cross-check the relative velocity distribution v(CH^+_{423}) - v(CH^+_{395}) is used. It should be zero because both lines originate from the same molecule species. The distribution is also narrower. A T-test shows that the difference of the mean of both distributions is not significantly different from 0 at a confidence level of 95%.

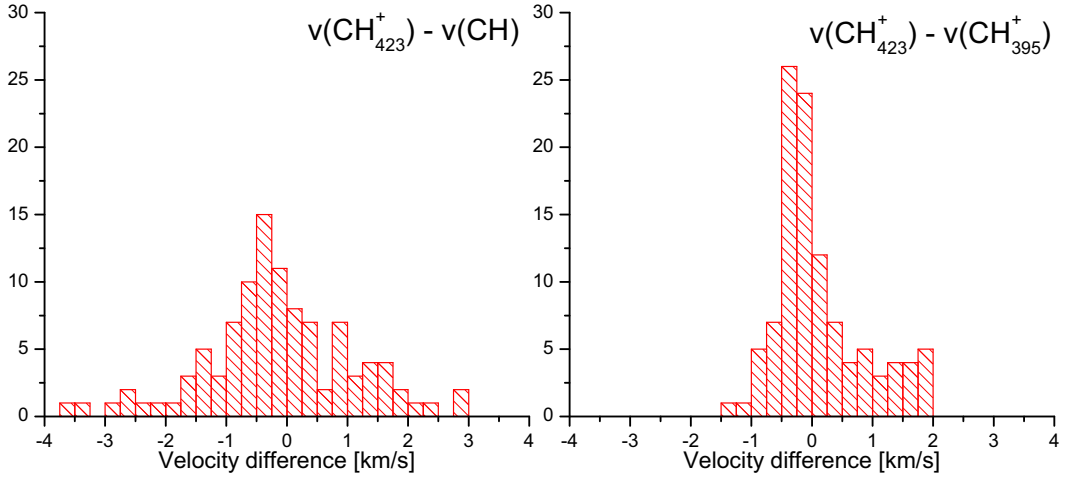

Figure 5.9: Histogram of the velocity difference of the CH^+ and the CH molecule (left) and two lines of the CH^+ molecule (right). A T-Test does not reject equal means (-0.11 ± 0.16 for v(CH^+_{423}) - v(CH) and 0.12 ± 0.07 for v(CH^+_{423}) - v(CH^+_{395})) at 95% confidence level.

5.2.2 Linewidths

The width of absorption lines is related to the velocity distribution of the absorbing matter, hence its temperature and turbulence.

The intrinsic linewidths of the CH_{430} and CH^+_{423} lines are plotted in fig. 5.10. The fit with fixed 0 offset gives a slope of 1.04 ± 0.04 with an R^2_{adj} of 0.84. The intrinsic linewidth is the measured line width from the fit to the absorption feature corrected for the instrumental line profile (Eq. 5.5). The intrinsic widths of both lines are almost the same with a small variation. The CH^+ line appears to be slightly broader.

The outliers to very high CH linewidths in the lower right of fig. 5.10 are observations towards HD 68450 and NGC 2546. Both data point belong to a group of lines of sight in a direction in between two spiral arms of our Galaxy that shows a remarkably low ratio of equivalent widths EW(CH^+)/EW(CH). This phenomenon is adressed in section 5.2.6.

The intrinsic width for both CH^+ lines from our sample is shown in fig. 5.11. The fit with fixed 0 offset gives a slope of 1.01 ± 0.02 with an R^2_{adj} of 0.97. The CH^+_{395} line is weaker than the CH^+_{423} line as can be seen from the equivalent width in tab. 5.2. This results in larger error bars for the weaker line in the plot.

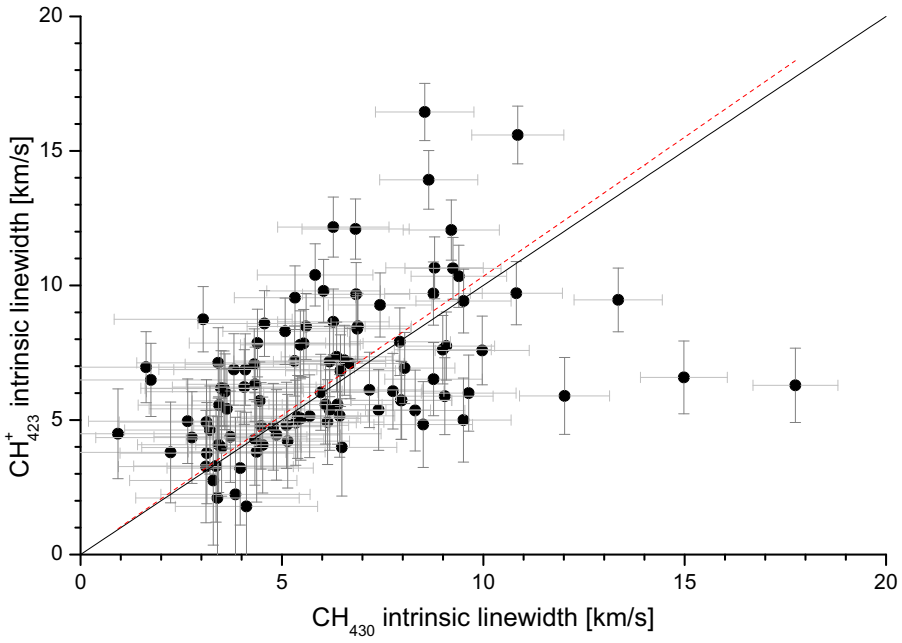

Figure 5.10: Intrinsic width of the CH_{430} line against the intrinsic width of the CH^+_{423} line. The fit (dashed red line) with fixed 0 offset gives a slope of 1.04 ± 0.04 with an R^2_{adj} of 0.84. The solid black line denotes unity.

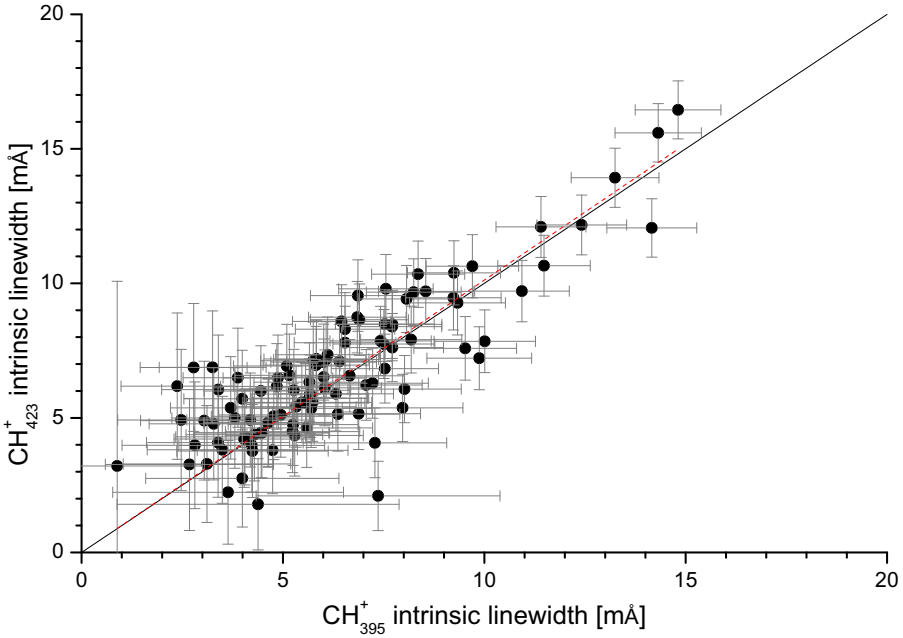

Figure 5.11: A comparison of the CH^+_{423} and the CH^+_{395} intrinsic line width gives a slope of 1.01 ± 0.02 with an R^2_{adj} of 0.97 (dashed red line). The solid black line denotes unity.

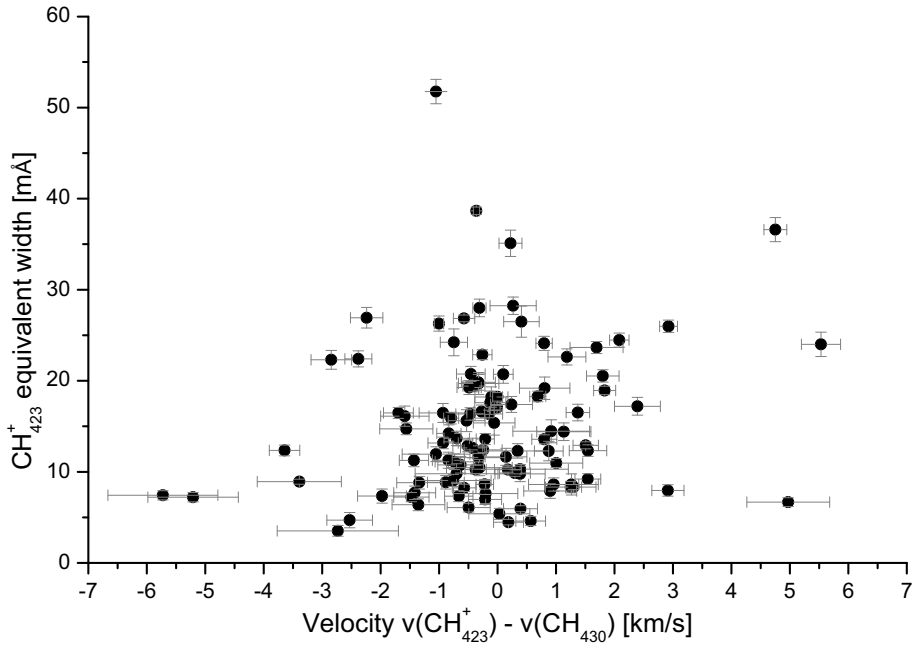

Figure 5.12: Plotted is the difference of the velocity of CH^+ and CH against the CH^+ equivalent width. A linear fit of the velocity difference against the equivalent width gives a slope of 0.49 ± 0.42 at an R^2_{adj} of 0.00.

5.2.3 Equivalent width and velocity

A correlation of equivalent width and velocity has been proposed as tracer for the influence of magnetic fields (Gredel, 1997). A plot of the velocity difference v(CH^+_{423}) - v(CH) against the equivalent width of CH^+_{423} is shown in fig. 5.12. The computed linear regression has a slope of 0.49 ± 0.42 at an R^2_{adj} of 0.00.
From this result it is clear that there is no correlation of equivalent width and velocity.

5.2.4 Equivalent width and extinction

The relation between equivalent width and extinction provides information about the distribution of the absorbing matter along the line of sight. The equivalent width is the integrated absorption for one spectral line of a molecule and the extinction is proportional to the amount of dust along the line of sight.
The equivalent width of the CH^+_{423} line is plotted against the visual extinction retrieved from the SIMBAD Astronomical Database in fig. 5.13. Only stars with Av > 0 in SIMBAD where used. The linear regression reveals a correlation of 8.23 ± 0.14 mÅ/mag at an $R^2_{adj} = 0.24$.
This can be compared to a linear fit of the CH_{430} equivalent line width against the visual extinction (Fig. 5.14) that gives a slope of 12.78 ± 0.15 mÅ/mag at an $R^2_{adj} = 0.58$. This correlation should exist because the CH molecule is abundant and exists along with dust that is responsible for the visual extinction. The fact that this physical correlation yields an R^2_{adj} of only 0.58 means that the correlation of visual extinction against CH^+ equivalent linewidth with an R^2_{adj} is most likely also valid.

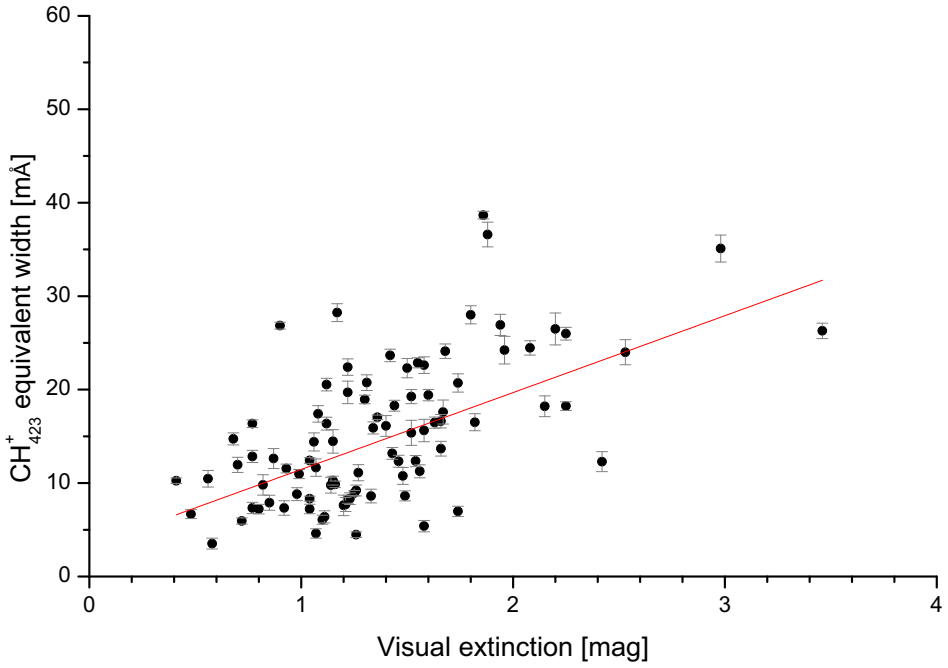

Figure 5.13: Plot of visual extinction against CH^+ equivalent linewidth. Linear fit gives a slope of 8.23 ± 0.14 at an $R^2_{adj} = 0.24$.

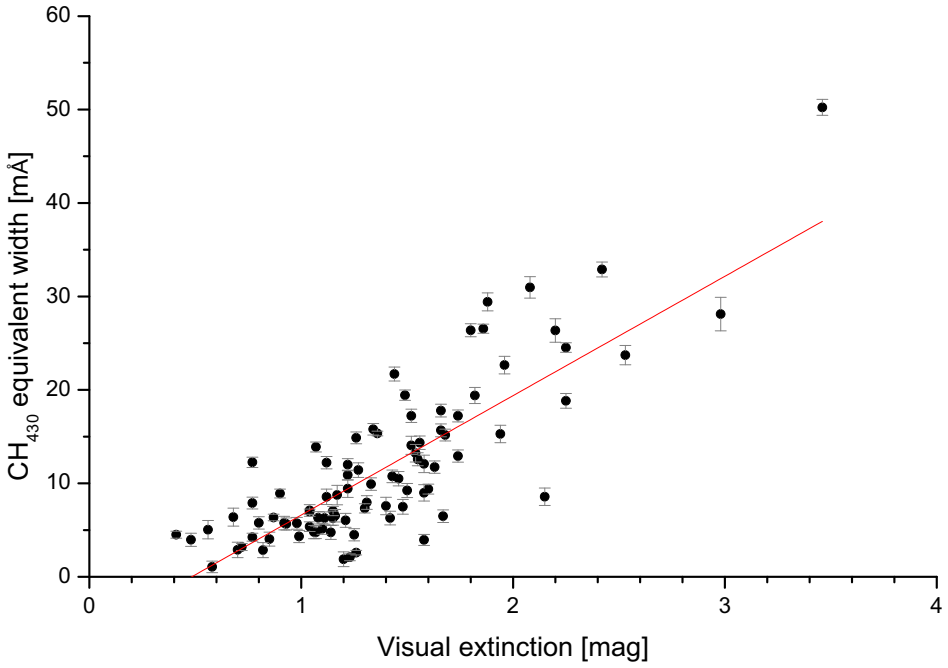

Figure 5.14: Plot of visual extinction against CH equivalent linewidth. Linear fit gives a slope of 12.78 ± 0.15 at an $R^2_{adj} = 0.58$.

5.2.5 Local subsample

To check if the length of the line of sight influences the correlations found in sections 5.2.2 and 5.2.4 one can form a local subsample of the dataset. Data points were selected into the subsample if the distance to the background star measured by Hipparcos is shorter than 500 parsec and the Hipparcos distance uncertainty is lower than 30 %.
The intrinsic line widths for this subsample are plotted in fig. 5.15. The fit with fixed 0 offset gives a slope of 1.11 ± 0.11 with an R^2_{adj} of 0.85 for the local subsample. The slope for the complete dataset was 1.04 ± 0.04 with an R^2_{adj} of 0.84. Slope and R^2_{adj} are identical to the complete sample within the uncertainties of the fits. The fit uncertainty for the subsample is greater due to the smaller number of data points.
The plots of equivalent width against extinction for this subsample are shown in fig. 5.16 and 5.17. Linear fit of visual extinction against CH^+ equivalent width gives a slope of 5.65 ± 3.41 at an $R^2_{adj} = 0.16$ for the local subsample. Linear fit of visual extinction against CH equivalent width gives a slope of 13.72 ± 4.10 at an $R^2_{adj} = 0.53$ for the local subsample. The slope standard errors are rather large, due to the small number of data points. Slope and R^2_{adj} for equivalent width against extinction are essentially the same as for the complete sample within the uncertainty of the fits (Tab. 5.3).

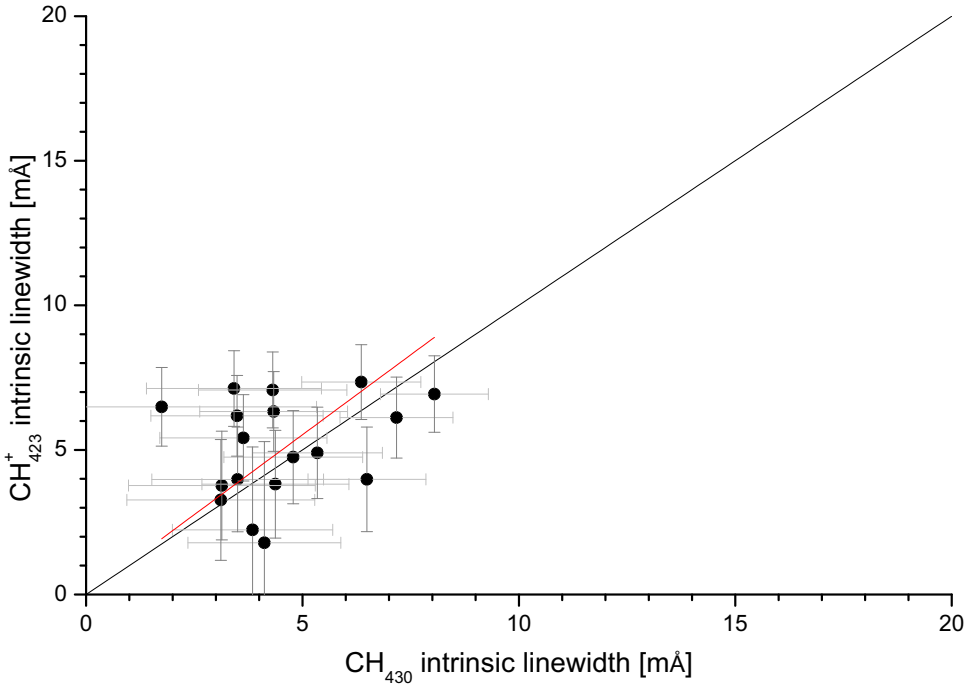

Figure 5.15: Intrinsic width of CH_{430} line against the intrinsic width of the CH^+_{423} line. The fit with fixed 0 offset gives a slope of 1.11 ± 0.11 with an $R^2_{adj} = 0.85$ for the local subsample. Compare to fig. 5.10 for the complete sample.

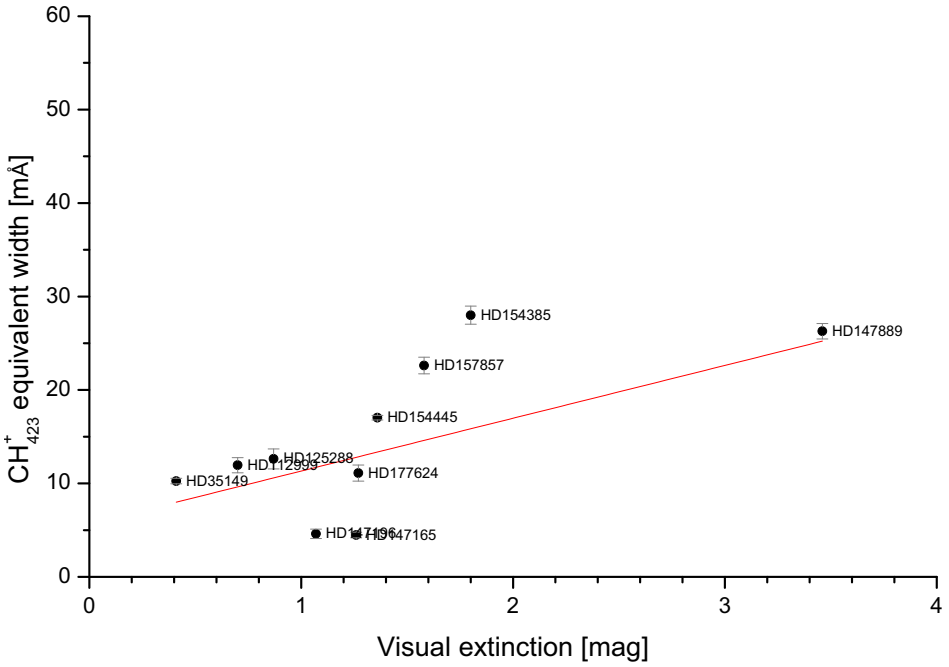

Figure 5.16: Linear fit of visual extinction against CH^+ equivalent width gives a slope of 5.65 ± 3.41 at an $R^2_{adj} = 0.16$ for the local subsample. Compare to fig. 5.13 for the complete sample.

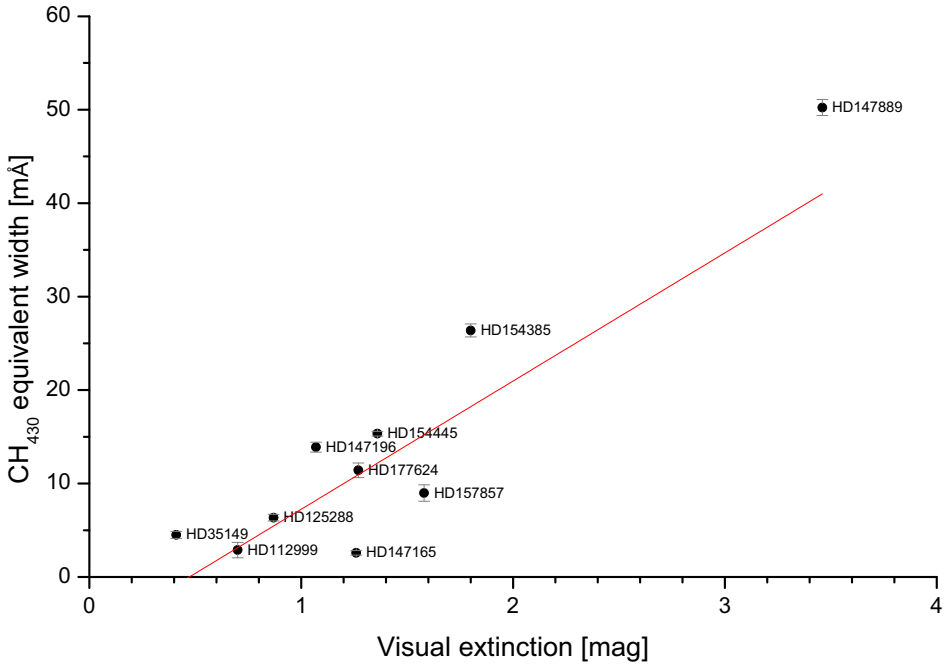

Figure 5.17: Linear fit of visual extinction against CH equivalent width gives a slope of 13.72 ± 4.10 at an $R^2_{adj} = 0.53$ for the local subsample. Compare to fig. 5.14 of the complete sample.

	Complete sample		500 pc subsample	
	slope	adj. R^2	slope	adj. R^2
$s_{intr}(CH^+)/s_{intr}(CH)$	1.04 ± 0.04	0.84	1.11 ± 0.11	0.85
$EW(CH^+)/Av$	8.23 ± 0.14	0.24	5.65 ± 3.41	0.16
EW(CH)/Av	12.78 ± 0.15	0.58	13.72 ± 4.10	0.53

Table 5.3: Comparison of correlations measured on the local 500 parsec subsample and the complete sample. Higher uncertainty in the subsample is due to the smaller number of data points used.

5.2.6 Galactic disc subsample

The influence of the galactic structure can be determined by forming a subsample with lines of sights within the galactic disc. The schematic structure of the Milky Way is shown in fig 5.18. For this subsample data points with a galactic latitude between -5 and 5 degrees were used. The result is shown in fig. 5.19.
Plotting the ratio of equivalent widths $EW(CH^+)/EW(CH)$ against the galactic longitude of the background star, a region with particularly low ratio can be identified (Fig. 5.19, upper plot). The corresponding range in longitude is the region in between two spiral arms. In this direction the equivalent widths for CH and CH^+ on their own are not unusual (Fig. 5.19, lower plot). Therefore the lower equivalent width ratio in the inter-arm direction is not a result of poor data quality.

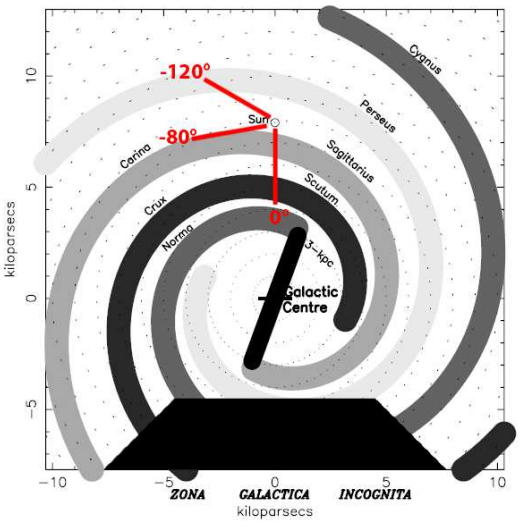

Figure 5.18: Schematic structure of the Milky Way from Vallée (2005). Red angles correspond to angles marked in fig. 5.19.

The correlation of the equivalent width ratio with the extinction tells us if CH^+ production is increased along dusty lines of sight with high extinction. This hypothesis can be ruled out as the slope of the fit is -0.13 ± 0.10 at an R^2_{adj} of 0.01 (Fig. 5.20).

The Hipparcos distance measurements for the background stars of the inter-arm lines of sight range up to several kiloparsec with increasing uncertainty. This means that these lines of sight are rather long and that they lead through a rather dark volume with less diffuse radiation compared to the lines of sight that lead through spiral arms.

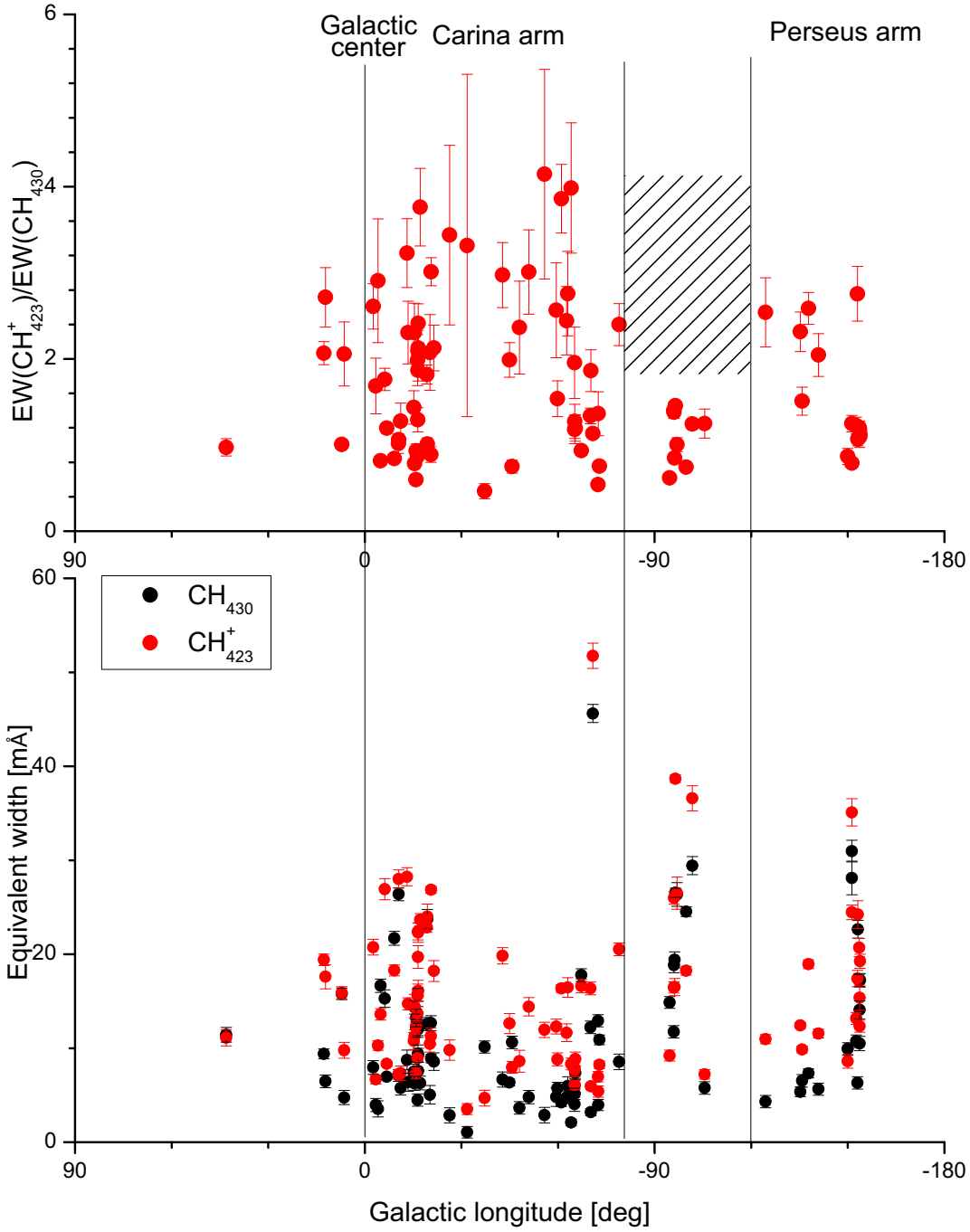

Figure 5.19: Top: Equivalent width of CH^+ divided by equivalent width of CH over the galactic latitude. The directions to the Carina arm and the Perseus spiral arm are marked. Hipparcos distance measurements for these datapoints range up to several kiloparsecs with increasing uncertainty. The relative width of CH^+ is weaker in the region between the Carina and the Perseus arm (hatched area). Bottom: Equivalent width of CH (black) and CH^+ (red). Data quality is reliable all over the covered region.

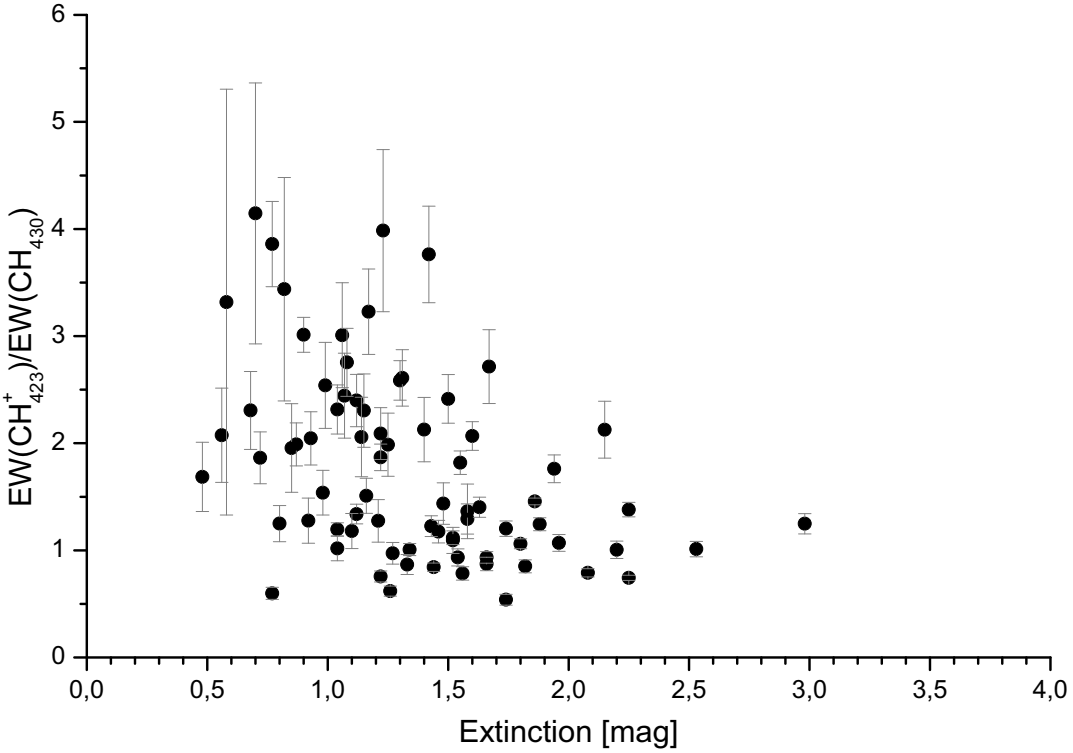

Figure 5.20: Equivalent width of CH^+ divided by equivalent width of CH over extinction. Linear fit gives a slope of -0.13 ± 0.10 at an R^2_{adj} of 0.01.

5.3 Discussion

A new dataset of CH and CH^+ absorption lines for a large number of lines of sight has been presented. Several hypotheses were tested on the dataset by calculating the significance of the tested correlation.

The first correlation tested should reveal if there is a difference in the velocities of CH^+ and CH. A different velocity of the two molecule species would mean that the absorbing matter resides on a different position along the line of sight or that CH^+ production has been powered from the kinetic energy of a shockwave.

A significant deviation from v(CH^+) - v(CH) = 0 could not be found in the dataset. This is in agreement with other samples, e.g. the high resolution observations of Lambert et al. (1990) towards ζ Ophiuchi, the ultra-high resolution observations of Crawford et al. (1994) and Crane et al. (1995).

The correlation of equivalent width and extinction that has been published by Gredel (1997) for five associations was confirmed as a general relation. This linear dependence of the CH^+ equivalent width from the extinction in the interstellar medium contradicts the hypothesis that CH^+ production is powered by shocks. There is no explanation why the number shocks on a line of sight should be correlated with the extinction. CH^+ is rather formed all along the line of sight than in singular shock fronts.

Measuring the width of the CH^+ and the CH line, it was found that the CH^+ lines appear to be slightly broader, which is consistent with the ultra-high resolution observations towards ζ Ophiuchi. In a calm, shock-free environment, this difference in width originates from different temperatures of the molecules. Different temperatures for both species mean, that CH^+ is formed in hotter, more energized regions while CH resides in colder areas of the interstellar medium.

Gredel (1997) uses a correlation of equivalent width and velocity to identify the influence of magnetic fields. The trajectories of the CH^+ ions are diverted in a magnetic field. Depending on the orientation towards the observer the absorption line could be different from the absorption line of the neutral, undisturbed molecule.

Such a correlation was not found, which confirms Gredels result from five associations with this more general sample. The correlation measure for this relation is very clear with an $R^2_{adj} = 0.00$. A general influence of magnetic fields on CH^+ production can be excluded.

A subsample of the dataset was formed using only short lines of sight to nearby stars within 500 parsec. The local subsample does not show a deviation from the complete sample. From this result, it is concluded that the CH^+ formation process is generally uniform and is not influenced by local effects.

Looking at a large sample of lines of sight, the most likely energy source for the production of CH^+ is the diffuse interstellar radiation field. The production of CH^+ powered by photons in the outer layer of fractal-like structured photon-dominated regions in the interstellar medium agrees with all results of this research. The inner part of the regions are shielded from the diffuse radiation, so that no CH^+ can be formed in these cooler, darker regions.

This scenario is consistent with a look at the ratio of CH^+ and CH equivalent widths in the Galaxy. In sec. 5.2.6, the ratio of CH and CH^+ equivalent width was plotted against the galactic longitude using only lines of sight within the galactic disc (Fig. 5.19).

In this plot CH^+ is clearly stronger in directions pointing to a spiral arm and weaker in the inter-arm region. CH^+ production is stronger, where the diffuse photon field is brighter, namely in the spiral arms. This shows that CH^+ formation depends on the diffuse photon field.

The energy available in a photon dominated region is large against the energy difference of the $^{13}CH^+$ and $^{12}CH^+$ molecules. The energy difference of the CH^+ isotopes equals to 35 K. Typical temperatures are expected of the order of a few thousand Kelvin. Crawford et al. (1994) derive upper limits from his ultra-high resolution observation towards ζ Ophiuchi of 2300 and 2500 K.

From eq. 5.3 we can calculate the influence of chemical fractionation. Assuming a temperature of 2000 K, the measurement of the carbon isotope ratio would be off from the true value by 1.8 %. This systematic error is small against the uncertainties of the measurements possible to date. Therefore the isotope ratio measured on CH^+ can be regarded as a reliable value for the particular line of sight.

Chapter 6

Conclusion

This thesis presents the design of BESO, the new high-resolution spectrograph for the Hexapod-Telescope. It points out the components being re-designed and upgraded over the design of FEROS that was used as a proven example for this new instrument.

The very effective collaboration with Landessternwarte Heidelberg facilitated the testing of components and the complete instrument, the transport and setup of the instrument until the start of service at the Cerro Armazones Observatory in Chile. This project has been presented at international conferences and could be concluded within the time frame and budget attributed.

The test data recorded with BESO at the observatory show that the performance of the optics slightly exceed the specifications. The first-light spectrum recorded with BESO was taken from the standard star Beta Ceti on August 30, 2008. The radial velocity of the star measured with BESO was 12.4 ± 0.1 km/s. The IAU reference for this star is 13.1 ± 0.2 km/s. The offset of this measurements from the reference value is attributed to a temperature drift of the instrument of a few Kelvin, which occurred because the observation was conducted during night time and the respective calibration frame was taken on the next day. For future science observations, the instrument will be temperature stabilized to ± 0.1 K/h and ± 0.5 K/day. Calibration frames will be taken before and after the observation. This will bring the instrument to the expected absolute precision.

Comparing our first-light observation to a spectrum taken one year earlier with FEROS at the observatory of La Silla, it is shown that the relative precision of the instrument and the quality of the recorded data is at the expected level.

Ruhr-Universität Bochum has now exclusive access to a very efficient, high-resolution full range optical spectrograph at one of the best locations for astronomical observations worldwide. As the central observational instrument at the Hexapod-Telescope, BESO puts the university in an outstanding position to carry out independent research campaigns in the years to come.

This research also analyzed the principles of the measurement of the isotope ratio in the interstellar medium using CH^+ absorption lines. Based on a new observational dataset, the most extensive dataset to date, it is shown on a reliable statistical basis that CH^+ is produced in an energetically hot environment powered by diffuse interstellar photons. In accordance with earlier results, turbulence in the interstellar medium or shock fronts or magnetic fields as major triggers of CH^+ production were excluded.
Forming a subset of lines of sight to nearby stars, it was verified that the measured properties are not influenced by local effects.
It was found that more CH^+ is produced along lines of sight towards the spiral arms of the Milky Way and less along lines of sight in between the arms of our Galaxy. This new insight illustrates that CH^+ production depends on the brightness of the diffuse interstellar photon field. More CH^+ is produced in the spiral arms where the interstellar photon field is brighter. The kinetic energy of the molecules in this environment and the energies of the diffuse photons are large compared to the energy difference of the molecules $^{12}CH^+$ and $^{13}CH^+$. The conclusion is that the isotope ratio measured on CH^+ absorption lines represents the true isotope ratio in the interstellar medium and that chemical fractionation affects the measurement only by up to a few percent.
This analysis consolidates the basis of the astrophysical isotope ratio measurement which is a key to understand the evolution of stars and the exchange of matter between stars and the interstellar medium. The dataset used for this research provides a useful basis to select lines of sight that are suitable for the isotope ratio measurement using ultra-high resolution spectroscopy.
Observations to measure the carbon isotope ratio for 45 lines with UVES at the ESO 8.2 m Very Large Telescope have been proposed. These future observations will determine if variations in the carbon isotope ratio are small-scale heterogeneities or if a gradient exists in the Galaxy.

Acknowledgment

The project to build a new spectrograph for the Cerro Armazones Observatory was based on the collaboration of Ruhr-Universität Bochum and Landessternwarte Heidelberg that has been established and supported by Prof. Chini, Prof. Appenzeller and his successor Prof. Quirrenbach. The project has been made possible by a grant from the Alfried Krupp von Bohlen und Halbach foundation.
The instrumental work would have been impossible without the contributions from all the experienced colleagues of Landessternwarte, European Southern Observatory and Ruhr-Universität. The installation of the instrument at the observatory has been supported by the colleagues at Universidad Católica del Norte who run the Cerro Armazones Observatory all around the year.
This research of the interstellar medium has been promoted to a large extent by Otmar Stahl through sharing his observational data and discussing the problem of chemical fractionation in the interstellar medium. Dominik Bomans and Martin Haas have provided important comments and ideas in the discussions.

Bibliography

D. W. Ball. *Field Guide to Spectroscopy*. The International Society for Optical Engineering, 2006.

S. Casassus, O. Stahl, and T. L. Wilson. Interstellar $^{12}C/^{13}C$ ratios through CHˆ+λλ 3957,4232 absorption in local clouds: incomplete mixing in the ISM. A&A, 441:181–194, October 2005. doi: 10.1051/0004-6361:20042149.

M. Centurion, C. Cassola, and G. Vladilo. The ˆ12ˆCHˆ+ˆ/ˆ13ˆCHˆ+ˆ ratio in the Coalsack. A&A, 302:243–+, October 1995.

P. Crane, D. L. Lambert, and Y. Sheffer. A Very High Resolution Survey of Interstellar CH and CH +. ApJS, 99:107–+, July 1995. doi: 10.1086/192180.

I. A. Crawford. Observations of interstellar lines towards HD 110432. *The Observatory*, 109:232–235, December 1989a.

I. A. Crawford. High-resolution observations of interstellar CH and CH(+) towards the Scorpius OB1 association. MNRAS, 241:575–593, December 1989b.

I. A. Crawford, M. J. Barlow, F. Diego, and J. Spyromilio. First Results from the UHRF / Ultra-High Observations of Interstellar CH CH+ and CN Towards Zeta-Ophiuchi. MNRAS, 266:903–+, February 1994.

ESO Astroclimatology website. http://www.eso.org/gen-fac/pubs/astclim/lasilla/diffrefr.html.

ESO MIDAS website. http://www.eso.org/midas/.

A. Faure and J. Tennyson. Electron-impact excitation of interstellar molecules. In A. Wilson, editor, *ESA Special Publication*, volume 577 of *ESA Special Publication*, pages 363–364, January 2005.

D. R. Flower and G. Pineau des Forets. C-type shocks in the interstellar medium: profiles of CHˆ+ and CH absorption lines. MNRAS, 297:1182–1188, July 1998.

R. Gredel. Interstellar CHˆ+ˆ in southern OB associations. A&A, 320:929–944, April 1997.

R. Gredel, E. F. van Dishoeck, and J. H. Black. The abundance of CH(+) in translucent molecular clouds - Further tests of shock models. A&A, 269:477–495, March 1993.

R. Gredel, G. Pineau des Forêts, and S. R. Federman. Interstellar CN toward CH^+-forming regions. A&A, 389:993–1014, July 2002. doi: 10.1051/0004-6361:20020543.

J. Greiner, W. Bornemann, C. Clemens, M. Deuter, G. Hasinger, M. Honsberg, H. Huber, S. Huber, M. Krauss, T. Krühler, A. Küpcü Yoldaş, H. Mayer-Hasselwander, B. Mican, N. Primak, F. Schrey, I. Steiner, G. Szokoly, C. C. Thöne, A. Yoldaş, S. Klose, U. Laux, and J. Winkler. GROND - a 7-channel imager. *ArXiv e-prints*, 801, January 2008.

M. E. Kaiser, E. L. Wright, and I. Hawkins. The interstellar (C-12)N/(C-13)N ratio toward Zeta Persei. ApJ, 379:267–270, September 1991. doi: 10.1086/170500.

D. L. Lambert, Y. Sheffer, and P. Crane. CN, CH, and CH(+) toward Zeta Ophiuchi. ApJ, 359:L19–L22, August 1990. doi: 10.1086/185786.

A. Megier, A. Strobel, A. Bondar, F. A. Musaev, I. Han, J. KreŁowski, and G. A. Galazutdinov. Interstellar Ca II Line Intensities and the Distances of the OB stars. *The Astrophysical Journal*, 634:451–458, November 2005. doi: 10.1086/496916.

National Institute of Standards and Technology website. http://physics.nist.gov/.

J. C. Pearson and B. J. Drouin. Laboratory Measurement of the J = 1-0 Transition of CH^+. ApJ, 647:L83–L86, August 2006. doi: 10.1086/506522.

Polymicro Technologies website. http://www.polymicro.com/products/opticalfibers/, date 09.09.2005.

Schott filter catalogue. http://www.schott.com/optics_devices/english/ download/ optical-glassdatasheetsv101007.xls.

SIMBAD Astronomical Database. http://simbad.u-strasbg.fr/simbad/.

O. Stahl, A. Kaufer, and S. Tubbesing. The FEROS spectrograph. In E. Guenther, B. Stecklum, and S. Klose, editors, *Optical and Infrared Spectroscopy of Circumstellar Matter*, volume 188 of *Astronomical Society of the Pacific Conference Series*, pages 331–+, 1999.

O. Stahl, S. Casassus, and T. Wilson. Interstellar $^{12}C/^{13}C$ from CH^+ absorption lines: results from an extended survey. A&A, 477:865–875, January 2008. doi: 10.1051/0004-6361:20078747.

I. Steiner. *Manual for the 'Bochum Echelle Spectrograph for the Cerro Armazones Observatory (BESO)'*. 2007.

I. Steiner, W. Seifert, O. Stahl, R. Lemke, R. Chini, and I. Appenzeller. *BESO: a high-resolution spectrograph for the Hexapod-Telescope*. Presented at the Society of Photo-Optical Instrumentation Engineers (SPIE) Conference. 2006.

I. Steiner, O. Stahl, W. Seifert, R. Chini, and A. Quirrenbach. *BESO: First light at the high-resolution spectrograph for the Hexapod-Telescope*. Presented at the Society of Photo-Optical Instrumentation Engineers (SPIE) Conference. 2008.

S. Udry, M. Mayor, E. Maurice, J. Andersen, M. Imbert, H. Lindgren, J.-C. Mermilliod, B. Nordström, and L. Prévot. 20 Years of CORAVEL Monitoring of Radial-Velocity Standard Stars. In J. B. Hearnshaw and C. D. Scarfe, editors, *IAU Colloq. 170: Precise Stellar Radial Velocities*, volume 185 of *Astronomical Society of the Pacific Conference Series*, pages 383–+, 1999.

A Unsöld. *Der neue Kosmos*. Springer Verlag, 1999.

J. P. Vallée. The Spiral Arms and Interarm Separation of the Milky Way: An Updated Statistical Study. AJ, 130:569–575, August 2005. doi: 10.1086/431744.

W. D. Watson. Interstellar molecule reactions. *Reviews of Modern Physics*, 48:513–552, October 1976a.

W. D. Watson. Interstellar molecule reactions. *Reviews of Modern Physics*, 48:513–552, October 1976b.

W. D. Watson, V. G. Anicich, and W. T. Huntress, Jr. Measurement and significance of the equilibrium reaction C-13/+/ + /C-12/O yields C-12/+/ + /C-13/O for alteration of the C-13/C-12 ratio in interstellar molecules. ApJ, 205:L165–L168, May 1976.

T. Weselak, G. A. Galazutdinov, F. A. Musaev, and J. Krełowski. The relation between CH and CN molecules and carriers of 5780 and 5797 diffuse interstellar bands. *Astronomy & Astropysics*, 484:381–388, June 2008. doi: 10.1051/0004-6361:20078304.

T. L. Wilson and R. Rood. Abundances in the Interstellar Medium. ARA&A, 32:191–226, 1994. doi: 10.1146/annurev.aa.32.090194.001203.